DIPLOMARBEIT

Asymptotic behavior of two-particle vertex functions in dynamical mean-field theory

Ausgeführt am Institut für Festkörperphysik
der Technischen Universität Wien

unter der Anleitung von
Ass. Prof. Dr. Alessandro Toschi und
Univ. Ass. Dr. Georg Rohringer

durch

Stefan Hummel

Zirbenweg 3/2/2
A-1220 Wien

Acknowledgements

First of all, I want to thank my supervisors Alessandro Toschi and Georg Rohringer for guiding me through my thesis and helping me in many different aspects of my work (even on weekends). Their permanent advise and support was an invaluable help for me writing my thesis, as well as for my understanding of different aspects of solid state physics. I owe my special thanks to Georg who, beside providing me with all information I have ever asked from the very beginning of my thesis, never got tired of answering all my questions (at any time) I had during my work. It was a pleasure for me to work with both of you! I am also very grateful to Karsten Held, who was giving me the warm welcome in his outstanding working group and who was also giving me the opportunity to present some of my pre-results at the joint annual meeting of the Austrian and Swiss physical society.

My very special thanks go to my family, who believed in me from the very beginning of my study to my final exam. They always supported me with their time, their advice and, as well, financially. I also want to thank my friends, simply because they were there for me. I would not have made it so far without my love, Karin Chmel. You are my inspiration and foothold each single day!

Abstract

Calculation of two-particle vertex functions is a fundamental ingredient for both postprocessing of results obtained by dynamical mean field theory (DMFT) as well as for diagrammatic extension of DMFT. The former allows for comparison with several state-of-the art scattering experiments beyond photoemission, like neutron, X-ray or electron-energy loss spectroscopies. As for the latter an efficient and precise calculation of irreducible two-particle vertex functions is a mandatory step for including spatial correlations on all length scales by means of the Dynamical Vertex Approximation. Hitherto, the considerable computational effort necessary for calculation of two-particle quantities has been one of the major limiting factors for both applications. This thesis aims to overcome these limitations by breaking the calculation down into two parts - (i) a full numerical calculation of the two-particle irreducible vertex functions in a low-frequency sector and (ii) a replacement of the irreducible vertex functions in the high-frequency sector with their corresponding asymptotic analytical expressions.

In the first part of this thesis, the theoretical framework for the calculation of two-particle quantities in the context of contemporary many-body quantum mechanics is illustrated. In chapter 3, the analytical expressions of the two-particle irreducible vertex functions in the high-frequency asymptotic regime are being calculated for all transferred bosonic frequencies and all channels. Following a previous work by Jan Kuneš (PRB, 2011) the downfolding terms, which are needed for the correction of the irreducible vertex functions calculated on a drastically truncated frequency space, have been derived. The numerical results for the high-frequency irreducible vertex functions and the irreducible vertex functions, calculated by means of the downfolding approach are given in chapter 4. Finally, conclusions are drawn and an outlook for future algorithmic improvements is given in chapter 5.

Kurzfassung

Die Berechnung von Zwei-Teilchen Vertex Funktionen ist ein wichtiger Schritt beim Auswerten von Ergebnissen aus Berechnungen mittels der dynamischen Molekularfeldtheorie (DMFT) auf Basis von Bethe-Salpeter Gleichungen, sowie für diagrammatische Erweiterungen der DMFT. Erstere ermöglichen direkte Vergleiche mit Ergebnissen aus Streuexperimenten wie Neutronen-, Röntgen- oder Elektronenenergieverlustspektroskopie (EELS), wohingegen letztere die Berechnung von nicht-lokalen Korrelationen, welche in DMFT nicht berücksichtigt werden, ermöglicht. Die Hauptschwierigkeit bei der Berechnung von Zwei-Teilchen Größen ist jedoch der beträchtliche numerische Aufwand. Die vorliegende Diplomarbeit versucht dieses Problem zu umgehen, indem - (i) die irreduziblen Vertex Funktionen auf einem sehr beschränkten, niedrigen Frequenzintervall numerisch berechnet werden und (ii) anschließend im restlichen Frequenzbereich die irreduziblen Vertex Funktionen durch ihre korrespondierenden asymptotischen Ausdrücke ersetzt werden.

Im ersten Teil dieser Arbeit werden zuerst die quantenfeldtheoretischen Methoden zur Berechnung von Zwei-Teilchen Größen beschrieben. In Kapitel 3 werden die analytischen Ausdrücke für die Zwei-Teilchen irreduziblen Vertex Funktionen für alle bosonischen Frequenzen und in allen Kanälen im asymptotischen Bereich berechnet. Anschließend werden, auf der Arbeit von Jan Kuneš (PRB, 2011) aufbauend, Downfolding-Terme abgeleitet und berechnet welche die, bei der Berechnung der Vertex Funktionen im niedrigen Frequenzintervall, entstandenen Fehler korrigieren. In Kapitel 4 werden die numerischen Ergebnisse für die irreduziblen Vertex Funktionen im asymptotischen Bereich sowie jene, durch ein Downfolding-Verfahren berechneten irreduziblen Vertex Funktionen im niedrigen Frequenzbereich dargestellt und analysiert. Zusammenfassend werden in Kapitel 5 Schlussfolgerungen aus den Ergebnissen, sowie Möglichkeiten zur weiteren Verbesserung der entwickelten Methode aufgezeigt.

Table of Contents

1 Introduction

In solid state physics, if one neglects relativistic effects, one easily can write down a "theory of everything" described by a Schrödinger's equation for the many-body system

$$H|\psi>= i\hbar\frac{\partial}{\partial t}|\psi> \tag{1}$$

with H, ψ being the (time-independent) many-body Hamiltonian and the many-body wave function respectively:

$$H(r_1, ..., r_n) = -\sum_{i=1}^{n}\frac{\hbar^2\nabla_i^2}{2m_i} + \sum_{i=1}^{n}U_i + \frac{1}{2}\sum_{i\neq j}^{n}U_{ij} \tag{2}$$

$$\psi := \psi(r_1, ...; r_n, t) \tag{3}$$

where n is the number of particles. These are completely general expressions, since U_i and U_{ij} might be any one and two-particle potential. In the case of solid state theory, U_i is the screened Coulomb potential of the atomic nuclei and U_{ij} the electron-electron interaction. In spite of the formal simplicity of this equation, its exact solution is only possible for a very few, simple cases. For systems where $n \leq 2$, equation (2) can be solved analytically. This is for example the case when calculating the energy levels of the hydrogen atom. For $n \leq 10$ one can at least solve (2) numerically. But in solid state physics, where $n \approx 10^{23}$, a numerical exact solution for (2) is evidently impossible. Therefore, reasonable approximations have to be performed to make this problem treatable, without the loss of the relevant physical information. For the investigation of the electronic structure of many-body systems in solid state physics, e.g., one of the most successful theories of the last fifty years is the density functional theory (DFT) [1,2]. With this theory, the properties of a many-electron system can be determined by using functionals of the spatially dependent electronic density. The very successful applications of DFT-based methods, as well as their flexibility to treat *ab-initio* quite complicate systems, has made these approaches the "standard" treatment in condensed matter. For these reasons, several numerical packages of high-reliability are developed around the world, two of which, among the most famous, here in Vienna (WIEN2k [3–5], VASP [6–9]). However, it is known that there are important classes of systems which cannot be treated even with the most advanced DFT-algorithms. One of the most important classes, where DFT delivers inaccurate or even wrong results, are the strongly correlated materials. These are systems, where the electron-electron interaction cannot be neglected (or considered too rudimentarily) anymore. On the other hand, electron-electron interactions are responsible (or assumed to be) for a number of astonishing effects in solid state systems, e.g. the Mott-Hubbard metal-insulator transition (MIT) in the vanadates [10], the colossal magnetoresistance of the manganites [11], the high-temperature superconductivity of cuprates [12] and (possibly) of iron pnictides [13]. In order to describe such systems using computational methods, one has to include explicitly the electronic correlation. Different approaches and approximations have been developed at this scope within existing theories, e.g. $LDA+U$ [14,15] for density

functional theory. However, instead of making substantial approximations for the electron-electron interaction (i.e., the U_{ij} term in Eq. 2) within DFT, many-body physicists have focused on the solution of model systems, which include the main physical aspects of the real system which are being investigated. For correlated systems, a widely used model is the Hubbard model [16], which in its simplest formulations, e.g. for a simple bond case on a cubic lattice reads:

$$\hat{H} = -t \sum_{<ij>\sigma} (c^{\dagger}_{i\sigma} c_{j\sigma} + c^{\dagger}_{j\sigma} c_{i\sigma}) + U \sum_{i\sigma\sigma'} c^{\dagger}_{i\sigma} c^{\dagger}_{i\sigma'} c_{i\sigma'} c_{i\sigma} \tag{4}$$

Here, t is the hopping parameter for adjacent sites ($< ij >$) and U the onsite Coulomb interaction. One of the advantages of using such a simpler modelization is the direct applicability of field-theoretical methods. In this respect, a major step forward in handling strongly correlated systems numerically has been achieved by the development of the Dynamical Mean Field Theory (DMFT) [17,18]. DMFT becomes exact in the limit of high spatial dimensions ($d \to \infty$) and already accounts for a large (local) part of electronic correlations. The key element of this method consists in mapping the (in general) intractable many-body lattice problem to a many-body local problem (impurity-model), which can be solved using various impurity solvers. The main approximation made in ordinary DMFT schemes is to assume the lattice self-energy to be a momentum-independent (local) quantity, which is evidently vigorously true only for $d = \infty$. Employing DMFT, it has been possible for the first time, to describe most of the radical changes upon going from a metal to a Mott insulator correctly. Beside the great success of this theory, there exist non-local correlation phenomena, e.g. in low-dimensional systems or in the proximity of (quantum) phase transitions, where DMFT is no longer applicable. There has been recent progress beyond DMFT through cluster extensions [19–22]. However, correlations included within cluster approaches are necessarily short-range in nature due to numerical limitations of the cluster size. A complementary route is provided by the diagrammatic extensions of DMFT, such as the dual-fermion method [23,24], one-particle irreducible approach [25], DMF^2RG [26] or the Dynamical Vertex Approximation ($D\Gamma A$) proposed by Toschi, Katanin and Held in 2007 [27,28]. All these diagrammatic extensions require the calculation of the local two-particle vertex function of DMFT as preliminary step. In the particular case of $D\Gamma A$, instead of assuming the self-energy to be local, one assumes the locality at an higher level of the diagrammatics, i.e., for the fully irreducible two-particle vertex, and consider all (local or nonlocal) self-energy diagrams that can be constructed from this vertex, e.g. by means of Bethe-Salpeter or Parquet equations. Therefore, it is clear that an efficient and precise calculation of the irreducible two-particle vertex is a mandatory step for the successful diagrammatic extension of DMFT by means of the Dynamical Vertex Approximation.

Let us also emphasize here that the calculation of irreducible vertex functions is also very important in the context of realistic applications of DMFT. In fact, local two-particle response functions are also sometimes calculated in DMFT.

However, the computation of non-local (two-particle) response functions is a more difficult venture. This is because nonlocal dynamic correlation functions of DMFT have to be calculated by means of the Bethe-Salpeter equations [29], if not using the alternative path recently proposed in [30], and hence also require the local irreducible vertex functions of DMFT. Such additional postprocessing effort would be highly rewarding in that, e.g., calculation of the dynamical susceptibilities allow for comparison with state-of-the art scattering experiments like neutron, x-ray or electron loss spectroscopies.

Hence, the calculations of two-particle vertex functions is a fundamental ingredient for both, postprocessing of DMFT results as well as diagrammatic extension of DMFT. Hitherto, the significant computational effort necessary for calculation of two-particle quantities has been one of the major limiting factors of the above mentioned procedures. Since one has (for time-independent Hamiltonians) to calculate the two-particle irreducible vertex functions in a 3D-frequency space, one usually has to restrict oneself to a low number of frequencies (throughout this thesis, numerical calculation of two-particle irreducible vertex functions has been performed on a maximum frequency space of 320 fermionic frequencies + 320 bosonic frequencies). In order to perform calculation of two-particle quantities (e.g. irreducible vertex functions) in larger frequency space within a reasonable time, other strategies than brute-force numerical inversion of the related equations (Bethe-Salpeter equations see Chap.2 and Chap.3) have to be considered [31,32]. In my thesis, I have followed a very promising strategy for calculation of two-particle irreducible vertex functions by means of dividing the frequency space in a low-frequency sector, where one still has to perform the numerical inversion of the regarding Bethe-Salpeter equations, and a high-frequency sector, where I have derived analytical expressions for the irreducible vertex functions in an asymptotical high-frequency form. Employing the downfolding scheme introduced by Jan Kuneš [33], I have used this asymptotical irreducible vertex functions in all channels and for all bosonic frequencies to calculate a correction term, which compensate for the error caused by the truncation of the numerical inversion on a low frequency range (e.g. 40 fermionic frequencies). In order to give a rather self-consistent explanation of this method, I have organized my thesis as follows:

In chapter 2, I have discussed the physical and mathematical importance of the calculation of two-particle quantities and explained the theoretical methods which I have used throughout my work. In the subsequent chapter, Chap.3, I have computed the analytical expressions of the two-particle irreducible vertex functions in the high-frequency asymptotic regime and derived the correction terms, which are needed for the correction of the irreducible vertex functions in all channels calculated on a drastically truncated frequency space. The last chapter (Chap.4) is devoted to the presentation of my numerical results. In particular, since the numerical analysis of the two-particle vertex function is rather new in the literature in the very first part of the chapter, I have analyzed the relation of the main frequency structure of the different vertices with the physics of the Mott-Hubbard transition. In the main part of Chap.4, I have

focused on the comparison of the numerical "exact" irreducible vertex functions with the asymptotical high frequency vertex functions and the truncated vertex functions. This way, I could demonstrate the strength of the herein developed downfolding procedure. At the same time I have also addressed limitations and possible strategies for an improvement of the methodology. Finally in Chap.5 I have briefly summarized the main results of this work as well as the perspectives for future developments.

2 Many-Body Green's functions

In this chapter, I will give an overview about quantum field theoretical methods beyond the standard one-particle level. I will first emphasize the importance of two-particle vertex functions within the framework of the dynamical mean field theory (DMFT) and as crucial input for diagrammatic extensions of DMFT. The second part is dedicated to the basic definitions of two-particle vertex functions and will provide us with the necessary tools for a derivation of the analytic expressions of the vertex functions in the asymptotic high-frequency regime.

2.1 Beyond two-point functions

Applying quantum field theoretical methods to condensed matter systems is usually done on a one particle level [34–36], i.e., one deals with so called two-point functions, e.g., the one-particle Green's function. Since the one-particle Green's function already contains important information about the physics of a correlated system (or model) such as the electronic density of states, or the spectral function, calculation of the one-particle Green's function has been hitherto one of the major tasks of computational material science. For example DMFT [17, 18, 37], which has become one of the most successful theories in describing strongly correlated electron systems, has been typically applied for calculation of the one-particle Green's function (and of course of the related self energy). In principle, also two-particle quantities can be calculated within DMFT [18]. This is usually done for the easiest cases of the optical and thermal conductivity, where vertex corrections are more easily neglected [18,38,39]. General calculation of spectral properties at the two-particle level is mostly restricted to local susceptibilities only. However, extending computational methods beyond the one-particle level is still of great interest for several reasons, e.g.,

- calculation of $\vec{q}$ dependent susceptibilities $\chi(\vec{q},\omega)$ allow for comparison to a much broader set of the experimental data than only photoemission, such as from inelastic neutron, Raman- or electron loss spectroscopy;
- monitoring of the divergencies of static susceptibilities as function of external control parameters (temperature, pressure, magnetic field, etc.) and the reciprocal lattice vector allows for an investigation of the (quantum) phase transitions and an unbiased determination of the order parameters;
- two-particle vertex functions are the basic ingredients for diagrammatic extension of DMFT, such as the dynamical vertex approximation (DΓA) [27, 28], the dual fermion approach (DF) [23, 24], the one-particle irreducible approach ($1PI$) [25] and the most recent DMF^2RG [26] approach.

Since the aim of this work is the calculation of (the asymptotic behavior of) two-particle vertex functions, we will consider the $n = 2$ case only, i.e., the diagrammatic approach at the two-particle (4-point functions) level. Although

we will keep the basic ideas of one-particle quantum field theory (e.g. partial summation, summation over Matsubara frequencies, etc.), as we will se, one has to be careful when transferring the conventional "diagrammatic recipes" beyond two-point functions.

Our starting point for the derivation of the most fundamental relations at the two-particle level will be the Hubbard model [16] on a simple cubic lattice

$$\hat{H}_{Hubbard} = -t \sum_{<ij>\sigma} \hat{c}^{\dagger}_{i\sigma} \hat{c}_{j\sigma} + U \sum_{i} \hat{n}_{i\uparrow} \hat{n}_{i\downarrow} \tag{5}$$

with next nearest neighbor hopping amplitude (t) and local Coulomb interaction U. Since, for the moment, we are interested in purely local quantities at the DMFT level, we will drop the lattice index i and keep the spin index only. Then, the most fundamental quantity for the two-particle level is the generalized two-particle susceptibility χ. It describes the propagation of two electrons added/removed into the system. Following the notation of Ref. [40], the definition is given as follows:

$$\begin{aligned} \chi_{\sigma_1\sigma_2\sigma_3\sigma_4}(\tau_1\tau_2\tau_3\tau_4) :=& < T(\hat{c}^{\dagger}_{\sigma_1}(\tau_1)\hat{c}_{\sigma_2}(\tau_2)\hat{c}^{\dagger}_{\sigma_3}(\tau_3)\hat{c}_{\sigma_4}(\tau_4)) > \\ & - < T(\hat{c}^{\dagger}_{\sigma_1}\hat{c}_{\sigma_2}) >< T(\hat{c}^{\dagger}_{\sigma_3}\hat{c}_{\sigma_4}) > . \end{aligned} \tag{6}$$

As we are dealing with a time-independent Hamiltonian, we can further simplify this expression to a function depending only on three times (τ_1,τ_2,τ_3,$\tau_4 = 0$). By employing a Fourier transformation, one ends up with an 3-frequency function, which will be our main object for all further considerations:

$$\begin{aligned} \chi(\nu\sigma,(\nu^{'}+\omega)\sigma^{'};(\nu+\omega)\sigma,\nu^{'}\sigma^{'}) = \int_0^{\beta} d\tau_1 d\tau_2 d\tau_3 \chi_{\sigma\sigma^{'}}(\tau_1,\tau_2,\tau_3) e^{-i\nu\tau_1} \\ e^{i(\nu+\omega)\tau_2} e^{-i(\nu^{'}+\omega)\tau_3} := \chi^{\nu\nu^{'}\omega}_{\sigma\sigma^{'}} \end{aligned} \tag{7}$$

This function can be represented diagrammatically as in Fig. 1: As one can

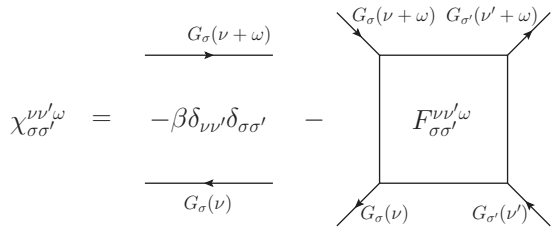

Figure 1: Generalized susceptibility in particle hole notation

see from its diagrammatic representation, the generalized susceptibilty can be split up into two separate parts, a disconnected and a connected one. Since the disconnected part comes from the two separate one particle propagations we can rewrite analytically the generalized susceptibility as:

$$\chi^{\nu\nu^{'}\omega}_{\sigma\sigma^{'}} = \chi_0^{\nu\nu^{'}\omega}\delta_{\sigma\sigma^{'}} - G_\sigma(\nu)G_\sigma(\nu+\omega)F^{\nu\nu^{'}\omega}_{\sigma\sigma^{'}}G_{\sigma^{'}}(\nu^{'})G_{\sigma^{'}}(\nu^{'}+\omega) \tag{8}$$

with

$$\chi_0^{\nu\nu'\omega} = -\beta G_\sigma(\nu) G_\sigma(\nu+\omega)\delta_{\nu\nu'}. \tag{9}$$

Due to this separation, the interpretation of the function F is straightforward. F contains all connected two particle diagrams. This includes all diagrams, which are not separated into two parts and, technically speaking, are defined 1-particle irreducible (1PI). We recall here, that also in the one-particle case, one can do such a separation. The main ingredients there, are the full Green's function G, a non-interacting Green's function G_0 and a self energy part Σ. However, in the two-particle case, the concept of irreducibility is more com-

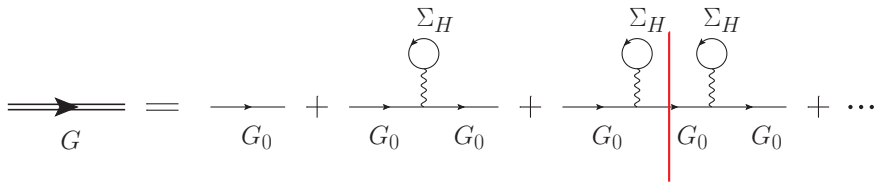

Figure 2: Illustration of the concept of reducibility/irreducibility at the one particle level. The given example is a diagrammatic representation of the Hartree approximation. The right-most diagram of the picture can be separated (red line) by cutting one bare Green's function line

plex, since to split a 2P-connected diagram in two parts one should cut at least *two* lines. From here, one can formally introduce the concept of 2P reducibility or irreducibility (2PI) of a diagram. Evidently, at the 2P-level, there are different ways how to realize this separation [41].

For instance, when looking at a generic connected two particle-diagram, we have two incoming and two outgoing legs. One possible way of cutting such a

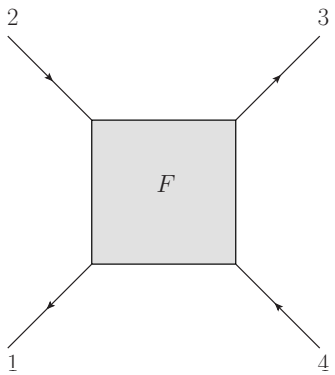

Figure 3: Generic 4-point function F

diagram, is by separating (1,2) from (3,4) by cutting two internal Green's function lines. A very basic example for such a diagram would be a two-particle bubble diagram of second order. Similarly, as in the one particle case, where we were able to find an equation of motion including the summation of irreducible

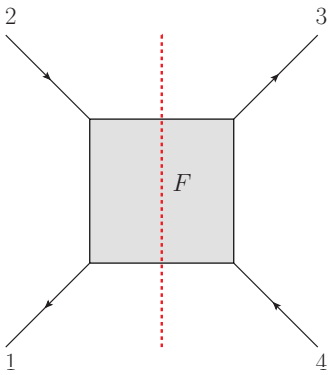

Figure 4: Vertex function vertical cut

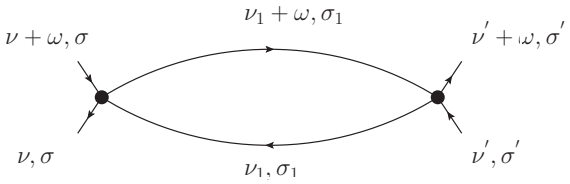

Figure 5: Bubble diagram

diagrams, i.e. Dyson's equation, we can perform a geometric resummation also for the two-particle case, which is known as the Bethe-Salpeter equation [29] As mentioned before, the separation of diagrams, and hence the concept of ir-

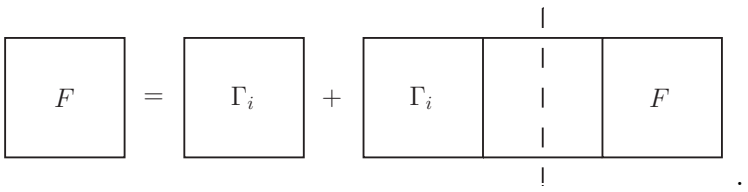

Figure 6: Diagrammatic representation of the Bethe-Salpeter equation. Γ_i is the vertex function, irreducible in channel i (described below); F is the full vertex function;

reducibility in the two-particle case is not unique:

For instance, we can also cut F in a "horizontal" way by separating (1,4) from (2,3). A basic example for such a diagram would be also a two-particle bubble diagram, but now vertically arranged. Moreover, there exists also a third option for cutting, namely (1,4) from (2,3), which is not shown here. Aiming at a more rigorous definition for such separation procedures, we introduce below the concept of irreducibility for general two-particle diagrams in a more formal way:

"A two-particle irreducible diagram is a two-particle diagram, which can not be separated by cutting two internal Green's function lines"

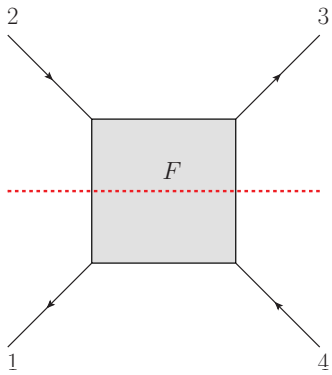

Figure 7: Vertex function with a horizontal cut

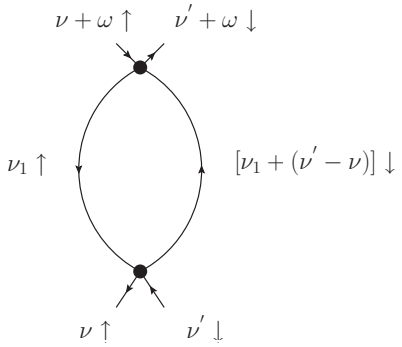

Figure 8: Vertical bubble-diagram

However, based on our previous considerations this definition of irreducibility at the 2P-level will be always connected to the "type" of separation. We usually refer to these three possible ways of separation with name of "channels" [41]. Considering our generic 4-point function, a separation (1,2) from (3,4) is defined as **"longitudinal particle-hole channel"**, whereas (1,4) from (2,3) defines the **"vertical particle-hole channel"**. As we will see later (see chapter 2.2) these two channels are linked together via a special symmetry relation. The third channel, (1,3) from (2,4) is somehow different, since it includes diagrams which consist particle particle propagation only and is therefore defined as **"particle-particle channel"**. To summarize the concept of irreducibility at the 2P-level, we recall that every connected diagram of F can be classified either:

- **fully irreducible** → diagrams, which cannot be split up into two parts by cutting two internal Green's function lines
  or as

- **reducible** (in a given channel) → diagrams, which can be split up into two parts by cutting two internal Green's function lines (according to the

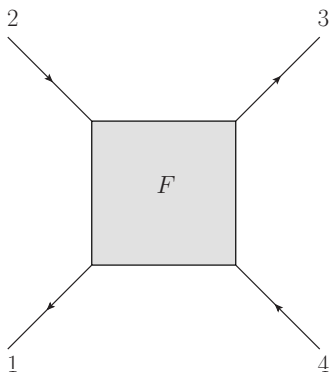

Figure 9: Generic 4-point function F

given channel)

There are no diagrams which are reducible in 2 channels [40]. Such classifications correspond essentially to the parquet equations [41–43].

Coming back to the Bethe-Salpeter equation, this can be defined in terms of the channel to be considered. Therefore, there exist three Bethe-Salpeter equations (one for each channel):

$$F = \Gamma_i + \sum\!\!\!\!\!\!\int \Gamma_i GGF \tag{10}$$

The interpretation of these kind of equations is now straightforward: F is the sum of all diagrams which are irreducible in the channel i + all diagrams which are reducible in this channel, for which we use the notation of Φ_i:

$$\Phi_i = \sum\!\!\!\!\!\!\int \Gamma_i GGF. \tag{11}$$

Before we can proceed in the analysis of two-particle diagrams we have to recall the definition of our main object, the Fourier transformed 4-point function.

$$\chi^{\nu\nu^{'}\omega}_{\sigma\sigma^{'}} = \int_0^\beta d\tau_1 d\tau_2 d\tau_3 \chi_{\sigma\sigma^{'}}(\tau_1,\tau_2,\tau_3) e^{-i\nu\tau_1} e^{i(\nu+\omega)\tau_2} e^{-i(\nu^{'}+\omega)\tau_3} \tag{12}$$

Due to energy conservation this is a three-frequency object. We note here that this specific convention for the frequency definition is known as **"particle-hole"** notation. In fact, with this notation, χ describes an electron with energy $\nu + \omega$ being scattered by a hole with energy $-\nu$ and ω being the total energy of this scattering process. However, since we only have to restrict ourself to energy conservation, we can find another equivalent frequency representation for χ, which we refer to a **"particle-particle"** notation.

$$\chi^{\nu\nu^{'}\omega}_{pp,\sigma\sigma^{'}} = \int_0^\beta d\tau_1 d\tau_2 d\tau_3 \chi_{\sigma\sigma^{'}}(\tau_1,\tau_2,\tau_3) e^{-i\nu\tau_1} e^{i(\omega-\nu^{'})\tau_2} e^{-i(\omega-\nu)\tau_3} \tag{13}$$

The physical motivation for this notation we can also see within the Fourier integral, where two electrons with energies $\nu^{'}$ and $\omega - \nu^{'}$ scatter. Due to the

fact that all scattering processes are included in the full Green's function, it is obviously possible to express the χ_{pp} in terms of χ_{ph} and vice versa.

$$\chi^{\nu\nu^{'}\omega}_{pp,\sigma\sigma^{'}} = \chi^{\nu\nu^{'}(\omega-\nu-\nu^{'})}_{ph,\sigma\sigma^{'}} \tag{14}$$

$$\chi^{\nu\nu^{'}\omega}_{ph,\sigma\sigma^{'}} = \chi^{\nu\nu^{'}(\omega+\nu+\nu^{'})}_{pp,\sigma\sigma^{'}} \tag{15}$$

2.2 Symmetries of Two-Particle Green's functions

For a better understanding of the properties of two-particle vertex functions and a more efficient numerical treatment, it is very useful to analyze the behavior of those functions under symmetry transformations. We will therefore give a brief overview on symmetry relations following Refs. [40] and [44] for two particle functions and their implications on the further calculations within this work (e.g., Spin diagonalization). Without loss of generality, we will report here the symmetry relations in the particle-hole frequency notation. Furthermore, although the equations reported below are shown for χ and Γ, obviously similar relations exist also for F, which can be found in Refs. [40] and [44].

2.2.1 Time-Reversal symmetry

Inside the time-ordering of Eq. 6 we can exchange the first two operators with the 3^{rd} and 4^{th}. Using the anticommutation relations for fermionic operators, one can permute the operators which, after Fourier transformation leads to

$$\chi^{(\nu^{'}+\omega)(\nu+\omega)(-\omega)}_{\sigma^{'}\sigma} = \chi^{\nu\nu^{'}\omega}_{\sigma\sigma^{'}} \tag{16}$$

2.2.2 Crossing-symmetry

As a consequence of the Pauli principle, we can derive a second symmetry relation, which is known as crossing-symmetry. The idea is that exchanging two identical particles - which means exchanging all arguments of the involved operators (i.e. the two c operators, should only change the sign of the vertex function. For parallel spin ($\sigma = \sigma^{'}$), exchanging $c_{\nu^{'}\sigma^{'}}$ and $c_{(\nu+\omega)\sigma}$ leads to

$$\begin{aligned}\chi^{\nu(\nu+\omega)(\nu^{'}-\nu)}_{\sigma\sigma} =& < c^{\dagger}_{\nu\sigma} c_{\nu^{'}\sigma} c^{\dagger}_{(\nu^{'}+\omega)\sigma} c_{(\nu+\omega)\sigma} > - \\ & < (c^{\dagger}_{\nu\sigma} c_{\nu^{'}\sigma}) >< c^{\dagger}_{(\nu^{'}+\omega)\sigma} c_{(\nu+\omega)\sigma} >\end{aligned} \tag{17}$$

The derivation of this relation can be found in Ref. [40] and [44]

$$\chi^{\nu(\nu+\omega)(\nu^{'}-\nu)}_{\sigma\sigma} = -\chi^{\nu\nu^{'}\omega}_{\sigma\sigma} + \chi^{\nu\nu^{'}\omega}_{0} + \chi^{\nu(\nu+\omega)(\nu^{'}-\nu)}_{0} \tag{18}$$

For antiparallel spin ($\sigma \neq \sigma^{'}$) the crossing symmetry reads as

$$\chi^{\nu(\nu+\omega)(\nu^{'}-\nu)}_{\sigma\sigma^{'},\sigma^{'}\sigma} = -\chi^{\nu(\nu+\omega)(\nu^{'}-\nu)}_{\sigma\sigma^{'}} + \chi^{\nu\nu^{'}\omega}_{0} \tag{19}$$

For a complete derivation of the crossing-symmetry, we refer to [40]

2.2.3 SU(2) symmetry

If the Hamiltonian does not contain terms which are breaking rotation symmetry (e.g. a magnetic field), one can show that every matrix element (and therefore also χ and F) has to fulfill spin-conservation. A further consequence is that we can find a relation of a χ and χ rotated by $\frac{\pi}{2}$, which reads as

$$\chi_{\sigma\sigma}^{\nu\nu'\omega} = \chi_{\sigma(-\sigma)}^{\nu\nu'\omega} - \chi_{\sigma(-\sigma)}^{\nu(\nu+\omega)(\nu'-\nu)} + \chi_{0}^{\nu\nu'\omega} \tag{20}$$

2.2.4 Spin-diagonalization

As a consequence of the SU(2)-symmetry, we can set up a new "spin-diagonal" basis for the longitudinal particle-hole irreducible channel Γ_{ph} and the particle-particle irreducible channel Γ_{pp} in terms of linear combinations of the two spin directions, ($\uparrow$,$\uparrow$) and ($\uparrow$,$\downarrow$). This can be done in the following way:

The basic four-point function (and therefore also Γ) has 2^4 possible spin combinations ($\uparrow$,$\downarrow$ for each outer leg). Since we are dealing with a SU(2) symmetric Hamiltonian, i.e. in the paramagnetic phase, we have spin conservation for all our diagrams. This reduces the number of combinations by 8. The remaining 8 combinations we can again reduce by 6 due to crossing symmetry. The two remaining combinations of spins are ($\uparrow\uparrow$;$\uparrow\uparrow$) and ($\uparrow\downarrow$;$\uparrow\downarrow$), which we indicate with a more compact notation as ($\uparrow\uparrow$) and ($\uparrow\downarrow$). Hence at the level of Γ, the remaining quantities we have to calculate are $\Gamma_{ph,\uparrow\uparrow}$, $\Gamma_{ph,\uparrow\downarrow}$,$\Gamma_{\overline{ph},\uparrow\uparrow}$,$\Gamma_{\overline{ph},\uparrow\downarrow}$,$\Gamma_{pp,\uparrow\uparrow}$,$\Gamma_{pp,\uparrow\downarrow}$.

If we further consider that the longitudinal channel can be transformed to the vertical one and vice versa via the crossing symmetry, the remaining quantities we have to calculate are $\Gamma_{ph,\uparrow\uparrow}$, $\Gamma_{ph,\uparrow\downarrow}$,$\Gamma_{pp,\uparrow\uparrow}$,$\Gamma_{pp,\uparrow\downarrow}$. This choice for the channel definition, however, is not the most optimal one, because they will be mixed by the Bethe-Salpeter equations. This problem can be avoided by performing a so called diagonalization in the spin-sector, which decouples all the four Bethe-Salpeter equations. The results of such diagonalization in the spin-sector is given by:

$$\begin{pmatrix} \Gamma_{ph,\uparrow\uparrow} \\ \Gamma_{ph,\uparrow\downarrow} \end{pmatrix} \Longrightarrow \begin{pmatrix} \Gamma_d = \Gamma_{ph,\uparrow\uparrow} + \Gamma_{ph,\uparrow\downarrow} \\ \Gamma_m = \Gamma_{ph,\uparrow\uparrow} - \Gamma_{ph,\uparrow\downarrow} \end{pmatrix} \tag{21}$$

$$\begin{pmatrix} \Gamma_{pp,\uparrow\uparrow} \\ \Gamma_{pp,\uparrow\downarrow} \end{pmatrix} \Longrightarrow \begin{pmatrix} \Gamma_t = \Gamma_{pp,\uparrow\uparrow} \\ \Gamma_s = 2\Gamma_{pp,\uparrow\downarrow} - \Gamma_{pp,\uparrow\uparrow} \end{pmatrix}. \tag{22}$$

The first pair is typically called the density-/magnetic-channel, i.e. $\Gamma_{d(ensity)}$ and $\Gamma_{m(agnetic)}$. The second pair, referring to the particle-particle sector is called singlet-/triplet-channel, i.e. $\Gamma_{s(inglet)}$ and $\Gamma_{t(riplet)}$. This notations and definitions will be used throughout the rest of this thesis.

3 Asymptotic behavior of vertex functions Γ

In the last chapter, we have derived symmetry relations for two-particle Green's and vertex functions, which can now be used for further analysis. The present chapter is dedicated to the derivation of the asymptotic behavior of the irreducible vertex function Γ. The concept of channel-dependent irreducibility of vertex functions (see also chapter 2.2) will be explicitly discussed and each channel will be analyzed separately. In particular, I will derive the expressions of the equations for the irreducible particle-hole and particle-particle channels in the asymptotic high-frequency regime in terms of the irreducible Γ's. I have also extended an algorithmic procedure for calculation of the low-frequency sectors of the irreducible Γ's based on the work of Jan Kuneš ([33]) to all channels and for all bosonic frequencies. A mathematical derivation based on the Lehmann representation [45] will be given in the last part of this chapter

As mentioned in the introduction, the main goal of this thesis is the calculation of the asymptotic behavior of two-particle irreducible vertex functions of DMFT. This represent a very important step for improving all algorithms using the Bethe-Salpeter equations in DMFT and for including non-local correlations on all length scales by means of diagrammatic extensions of DMFT [18, 23, 27, 33, 37]. Following Refs. [40, 41, 44], we start from the Bethe Salpeter equations

$$F = \Gamma_i + \Phi_i \tag{23}$$

where Γ_i and Φ_i are the irreducible part and reducible part of channel i ($i = (ph, \overline{ph}, pp)$) respectively and the Parquet equation [41–43]

$$F = \Lambda + \Phi_{ph} + \Phi_{\overline{ph}} + \Phi_{pp}, \tag{24}$$

where Λ is the fully two-particle irreducible vertex. Combining both equations (23) and (24) leads to

$$\Gamma_{ph} = \Lambda + \Phi_{\overline{ph}} + \Phi_{pp} \tag{25}$$

$$\Gamma_{\overline{ph}} = \Lambda + \Phi_{ph} + \Phi_{pp} \tag{26}$$

$$\Gamma_{pp} = \Lambda + \Phi_{ph} + \Phi_{\overline{ph}} \tag{27}$$

for the vertex functions irreducible in channel $i = (ph, \overline{ph}, pp)$.

Similarly as $\chi^{\nu\nu'\omega}$, obviously Γ as well as Λ and Φ are 3-frequency functions. In order to study the asymptotic frequency behavior of the irreducible vertices Γ_i, we consider the 3-dimensional frequency space, spanned by the two fermionic frequencies ν and ν' and the bosonic frequency ω. In fact, as we will show explicitly in the following, the asymptotic behavior of $\Gamma_i^{\nu\nu'\omega}$ is not uniform in the (ν, ν', ω)-space, i.e., it strongly depends on the direction in this space when approaching ∞ [40]

As mentioned in the previous chapter, since we are considering the paramagnetic phase only, the relevant spin combinations are

$(\uparrow;\uparrow)$ and $(\uparrow;\downarrow)$.

Furthermore, as discussed in chapter 2.2 and [40], taking into account the crossing symmetry, we can restrict ourselves to the calculation of the longitudinal particle-hole irreducible channel (Eq. 25) and the particle-particle irreducible channel (Eq. 27). As for the spin sectors (d,m,s,t), it is convenient to study the asymptotic behavior of Γ_{ph} and Γ_{pp} in terms of $(\uparrow;\uparrow)$ and $(\uparrow;\downarrow)$ spin channels and go back to the spin-diagonalized basis (d,m,s,t), introduced in Chap. 2.2 later. For the study of the asymptotic behavior of the vertex functions, we introduce the following notation, where the exact way the high frequency limit is taken has to be explicitly specified[1]:

$$\Gamma^{\nu\nu'\omega}_{i,asympt} := \{\Gamma_i^{\nu\nu'\omega} : \lim_{\nu\nu'\omega\to\infty} \Gamma_i^{\nu\nu'\omega}\} \tag{28}$$

3.1 Longitudinal Particle-Hole Channel

For calculation of this channel we use its natural frequency notation, i.e. the particle-hole notation (see Eq. 12. As mentioned above, we first will calculate all relevant diagrams for this channel in the $(\uparrow;\uparrow)$ and $(\uparrow;\downarrow)$ spin sectors and finally use the spin-diagonalized basis in order to get the asymptotic behavior of $\Gamma_{d(ensity)}$ and $\Gamma_{m(agnetic)}$. We will now study each part of the right hand side of Eq. 25 separately.

3.1.1 fully irreducible diagrams Λ

Let us start analyzing the lowest order diagrams:

$(\uparrow\uparrow)$

We can immediately see that, due to Pauli's principle, there is no contribution to Λ_{asympt} at the first order in U (two electrons with parallel spin cannot exist at the same place and at the same time).

$(\uparrow\downarrow)$

For the antiparallel spin-case, the lowest order diagram does contribute to the asymptotic fully-irreducible vertex (see Fig. 10 for $\sigma \neq \sigma'$ gives a constant U).

Moreover, for both spin combinations, all higher-order diagrams decay at least as $\frac{1}{\nu}$. If we consider the subsequent order in perturbation theory for Γ, this is

[1]The asymptotic high-frequency behavior of $\Gamma_i^{\nu\nu'\omega}$ is not uniform in the (ν,ν',ω)-space but strongly depends on the direction in this space when approaching ∞. In this sense, $\Gamma^{\nu\nu'\omega}_{i,asympt}$ contains all diagrams of $\Gamma_i^{\nu\nu'\omega}$, which do not vanish when approaching ∞ along certain directions in the (ν,ν',ω)-space.

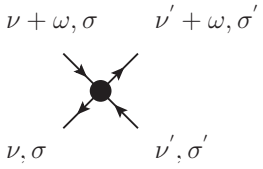

Figure 10: Lowest order diagram for Λ: for σ=$\sigma^{'}$ this diagram doesn't exist

given by the 4th order envelope diagram (Fig. 11). Our numerical evaluation of this diagram demonstrate a uniform asymptotic behavior decaying at least as $\frac{1}{\nu}$. Evidently, higher order diagrams will display an even stronger decay.

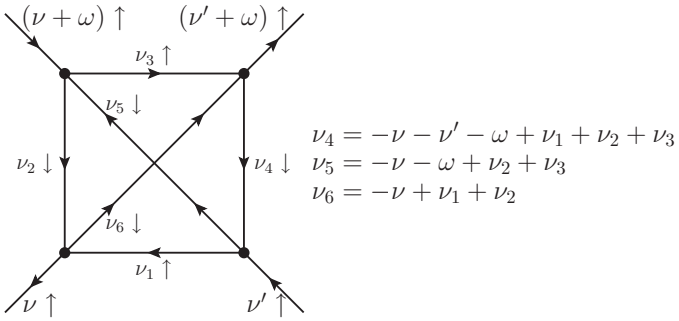

Figure 11: An example of a 4th order envelope diagram for $(\uparrow\uparrow)$

Therefore, the only contribution to the asymptotic behavior of Λ is given by the lowest order diagram in the $(\uparrow,\downarrow)$ shown in Fig. 10. The corresponding sign can easily be calculated by explicitly applying Wick's theorem in the perturbation expansion and considering the anticommutation relations for fermionic operators. This yields that the diagram Fig. 10 contributes with a + sign and hence:

$$\Lambda_{\uparrow\downarrow,asympt} = +U. \tag{29}$$

3.1.2 reducible vertical particle-hole diagrams $\Phi_{\overline{ph},asympt}$

$(\uparrow\uparrow)$

The lowest order diagram which is contributing to the asymptotics is the vertical particle-hole bubble (Fig. 12) In terms of Green's functions, this reads

$$P_1(\nu,\nu^{'}) = -\frac{U^2}{\beta}\sum_{\nu_1} G(\nu_1)G(\nu_1+\nu^{'}-\nu). \tag{30}$$

If we now look at the asmyptotic behavior of this diagram, we find that for keeping ν constant, this diagram vanishes for $\nu^{'}\to\infty$

$$\lim_{\nu^{'}\to\infty} P_1(\nu,\nu^{'}) = 0.$$

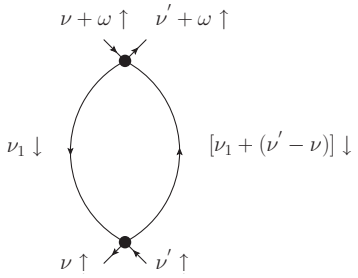

Figure 12: Second order vertical particle-hole reducible diagram

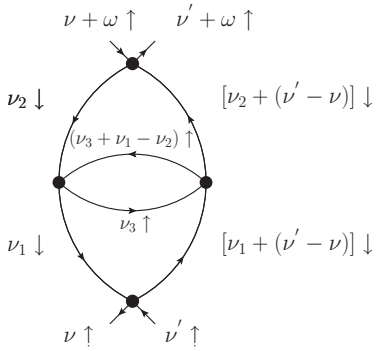

Figure 13: 4th order vertical particle-hole reducible diagram

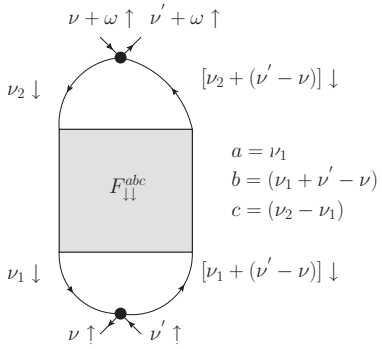

Figure 14: General vertical particle-hole reducible diagram with vertex insertions

Obviously, we will get the same result if we exchange $\nu^{'}$ by ν, i.e., $\nu \to \infty$. However, if we choose the path $\nu = \nu^{'}$ the vertical bubble diagram will not vanish anymore. In fact, we can write $P_1(\nu, \nu^{'})$ as a function of only one bosonic frequency, $\nu^{'} - \nu$

$$P_1(\nu, \nu^{'}) = -\frac{U^2}{\beta} \sum_{\nu_1} G(\nu_1) G(\nu_1 + \nu^{'} - \nu) = +U^2 \chi_0(\nu^{'} - \nu) \tag{31}$$

In a similar way, we can now analyze also higher order diagrams of this class (i.e. vertical particle-hole bubble with vertex insertions) and according to Fig. (13, 14) this leads to

$$P_2(\nu, \nu^{'}) = +\frac{U^2}{\beta^2} \sum_{\nu_1 \nu_2} G(\nu_1) G(\nu_1 + \nu^{'} - \nu) F^{\nu_1(\nu_1+\nu^{'}-\nu)(\nu_2-\nu_1)}_{\downarrow\downarrow} G(\nu_2) G(\nu_2 + \nu^{'} - \nu). \tag{32}$$

Hence the contribution of the diagram shown in Fig. 14 can be also written as effective one-frequency function $P_2(\nu^{'} - \nu)$. Summing up all contributions to

$\Phi_{\overline{ph}\uparrow\uparrow,asymp}$ (Eq. 30, Eq. 32) leads to

$$\Phi_{\overline{ph}\uparrow\uparrow,asympt} = -\frac{U^2}{\beta^2}\sum_{\nu_1\nu_2}[\beta G(\nu_1)G(\nu_1+\nu^{'}-\nu)\delta_{\nu_1\nu_2} - G(\nu_1)G(\nu_1+\nu^{'}-\nu)F_{\downarrow\downarrow}^{\nu_1(\nu_1+\nu^{'}-\nu)(\nu_2-\nu_1)}G(\nu_2)G(\nu_2+\nu^{'}-\nu)]. \tag{33}$$

According to Eq. 9, we can write the first part as $-\chi_0^{\nu_1\nu_2(\nu^{'}-\nu)}$. For the second part, we use the crossing symmetry and write

$$F_{\downarrow\downarrow}^{\nu_1(\nu_1+\nu^{'}-\nu)(\nu_2-\nu_1)} = -F_{\downarrow\downarrow}^{\nu_1\nu_2(\nu^{'}-\nu)}. \tag{34}$$

For the SU(2) symmetric case, $\chi_{\downarrow\downarrow}^{\nu_1\nu_2(\nu^{'}-\nu)} = \chi_{\uparrow\uparrow}^{\nu_1\nu_2(\nu^{'}-\nu)}$ and we finally end up with the following expression for $\Phi_{\overline{ph}\uparrow\uparrow,asympt}$

$$\Phi_{\overline{ph}\uparrow\uparrow,asympt} = +\frac{U^2}{\beta^2}\sum_{\nu_1\nu_2}\chi_{\uparrow\uparrow}^{\nu_1\nu_2(\nu^{'}-\nu)} = U^2\chi_{\uparrow\uparrow}(\nu^{'}-\nu). \tag{35}$$

$(\uparrow\downarrow)$

We again start with the bubble-diagram without any vertex insertions (Fig. 15) and get the same asymptotic contribution as for the $(\uparrow\uparrow)$ case

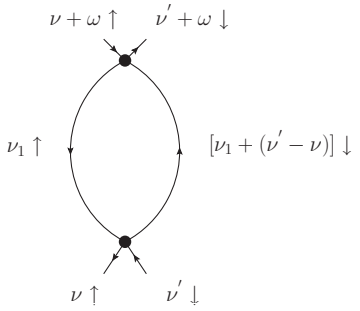

Figure 15: Second order vertical particle-hole reducible diagram

$$P_3(\nu^{'}-\nu) = -\frac{U^2}{\beta}\sum_{\nu_1}G(\nu_1)G(\nu_1+\nu^{'}-\nu). \tag{36}$$

Considering all higher order diagrams (e.g. Figs. (16),(17)), this again leads to a very similar expression as for the $(\uparrow\uparrow)$ case namely,

$$P_4(\nu^{'}-\nu) = +\frac{U^2}{\beta^2}\sum_{\nu_1\nu_2}G(\nu_1)G(\nu_1+\nu^{'}-\nu)F_{\uparrow\downarrow}^{\nu_1(\nu_1+\nu^{'}-\nu)(\nu_2-\nu_1)}G(\nu_2)G(\nu_2+\nu^{'}-\nu) \tag{37}$$

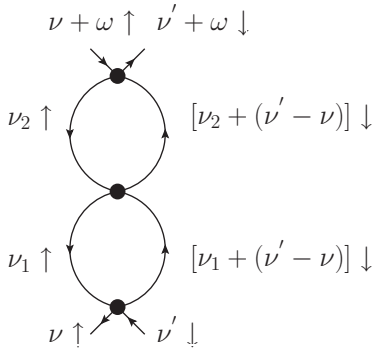

Figure 16: 4th order vertical particle-hole reducible diagram

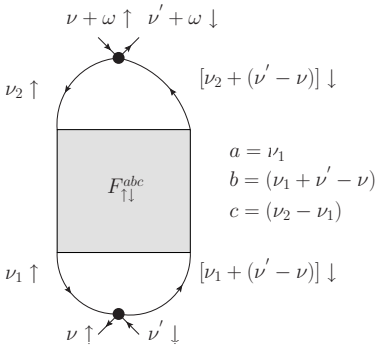

Figure 17: General vertical particle-hole reducible diagram with vertex insertions

Summing up all terms leads to

$$\begin{aligned}\Phi_{\overline{ph}\uparrow\downarrow,asympt} = &-\frac{U^2}{\beta^2}\sum_{\nu_1\nu_2}[\beta G(\nu_1)G(\nu_1+\nu'-\nu)\delta_{\nu_1\nu_2} \\ &- G(\nu_1)G(\nu_1+\nu'-\nu)F_{\uparrow\downarrow}^{\nu_1(\nu_1+\nu'-\nu)(\nu_2-\nu_1)}G(\nu_2)G(\nu_2+\nu'-\nu)].\end{aligned} \tag{38}$$

As for the $(\uparrow\uparrow)$, we want to find an expression only in terms of χ_0 and χ. Applying the SU(2) symmetry

$$F_{\uparrow\downarrow}^{\nu_1(\nu_1+\nu'-\nu)(\nu_2-\nu_1)} = F_{\uparrow\uparrow}^{\nu_1(\nu_1+\nu'-\nu)(\nu_2-\nu_1)} + F_{\uparrow\downarrow}^{\nu_1\nu_2(\nu'-\nu)}. \tag{39}$$

and using again the crossing symmetry for the $(\uparrow\uparrow)$-vertex yields

$$F_{\uparrow\downarrow}^{\nu_1(\nu_1+\nu'-\nu)(\nu_2-\nu_1)} \overset{crossing-symmetry}{\overset{!}{=}} -F_{\uparrow\uparrow}^{\nu_1\nu_2(\nu'-\nu)} + F_{\uparrow\downarrow}^{\nu_1\nu_2(\nu'-\nu)}. \tag{40}$$

Now we can write Eq. 38 in terms of χ only, ending up with

$$\begin{aligned}\Phi_{\overline{ph}\uparrow\downarrow,asympt} =& +\frac{U^2}{\beta^2}\sum_{\nu_1\nu_2}(\chi_{\uparrow\uparrow}^{\nu_1\nu_2(\nu'-\nu)} - \chi_{\uparrow\downarrow}^{\nu_1\nu_2(\nu'-\nu)}) \\ =&U^2[\chi_{\uparrow\uparrow}(\nu'-\nu) - \chi_{\uparrow\downarrow}(\nu'-\nu)] \\ =&U^2\chi_m(\nu'-\nu).\end{aligned} \tag{41}$$

3.1.3 reducible particle-particle diagrams Φ_{pp}

For this section, we will slightly modify the way of drawing our diagrams and put the outer "particle-legs" on the upper side, and the outer "hole-legs" on the lower side. It is important to notice however, that we still keep the particle-hole frequency notation used in the previous section. The above mentioned step is only a "trick" for better visualization of the particle-particle reducible diagrams.

$(\uparrow\uparrow)$

The lowest order contribution has the shape shown in Fig. 18 In contrast to

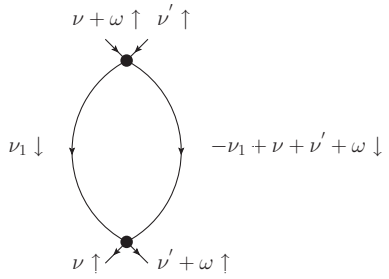

Figure 18: This diagram cannot exist, due to Pauli's principle

the vertical particle-hole diagrams, we now have to consider the Pauli principle, where two fermions with the same spin cannot be at the impurity at the same time. If we look at the particle-particle bubble diagram in Fig. 18, we immediately see, that for the $(\uparrow\uparrow)$ case, there is no contribution to the asymptotics due to Pauli's principle.

$(\uparrow\downarrow)$

For the $(\uparrow\downarrow)$ case, the lowest order diagram has the following form (Fig. 19). In terms of Green's functions, this reads

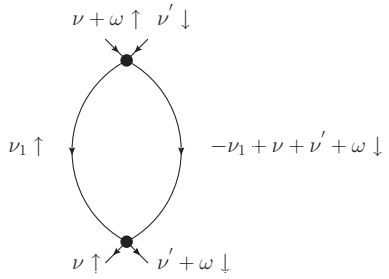

Figure 19: Second order vertical particle-particle reducible diagram

$$\begin{aligned} P_5(\nu+\nu'+\omega) &= -\frac{U^2}{\beta}\sum_{\nu_1} G(\nu_1)G(-\nu_1+\nu+\nu'+\omega) \\ &= U^2\chi_0(\nu+\nu'+\omega) \end{aligned} \tag{42}$$

If we now look at the asymptotic frequency behavior, we find a non vanishing contribution of Fig. 19 for

$$\nu+\nu'+\omega = const, \tag{43}$$

assuming a maximum for

$$\nu+\nu'+\omega = 0. \tag{44}$$

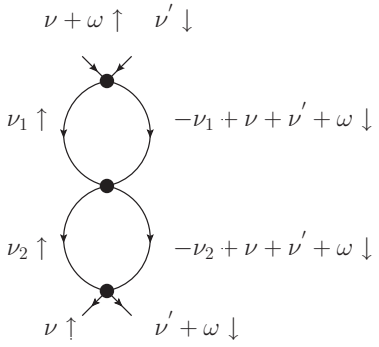

Figure 20: 4th order vertical particle-particle reducible diagram

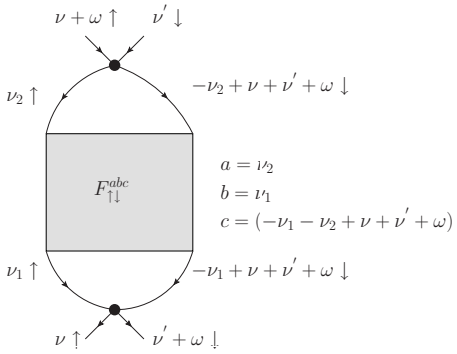

Figure 21: General vertical particle-particle reducible diagram with vertex insertions

Considering higher order terms (Fig. 20, 21), we find a general expression for such contributions

$$P_6(\nu,\nu',\omega) = +\frac{U^2}{\beta^2}\sum_{\nu_1\nu_2} G(\nu_1)G(\nu_2)F_{\uparrow\downarrow}^{\nu_2\nu_1(-\nu_1-\nu_2+\nu+\nu'+\omega)} \\ G(-\nu_1+\nu+\nu'+\omega)G(-\nu_2+\nu+\nu'+\omega). \tag{45}$$

Summing up all contributions of the reducible particle-particle channel leads to Eq. 46

$$\Phi_{pp\uparrow\downarrow,asympt} = -\frac{U^2}{\beta^2}\sum_{\nu_1\nu_2}[-\beta G(\nu_1)G(-\nu_1+\nu+\nu'+\omega)\delta_{(-\nu_1-\nu_2+\nu+\nu'+\omega)0} \\ + G(\nu_1)G(\nu_2)F_{\uparrow\downarrow}^{\nu_2\nu_1(-\nu_1-\nu_2+\nu+\nu'+\omega)}G(-\nu_1+\nu+\nu'+\omega)G(-\nu_2+\nu+\nu'+\omega)]. \tag{46}$$

If we rewrite this equation in terms of χ we can write $\Phi_{pp\uparrow\downarrow,asympt}$ as Eq. 47.

$$\Phi_{pp\uparrow\downarrow,asympt} = -\frac{U^2}{\beta^2}\sum_{\nu_1\nu_2}[\chi_{\uparrow\downarrow}^{\nu_2\nu_1(-\nu_1-\nu_2+\nu+\nu'+\omega)} + \\ \beta G(\nu_1)G(-\nu_1+\nu+\nu'+\omega)\delta_{(-\nu_1-\nu_2+\nu+\nu'+\omega)0}]. \tag{47}$$

Analyzing the diagrams in Fig. 21 and Fig. 17 for fixed ω, we see that the main contribution of the reducible vertical particle-hole channel is along the diagonal $\nu=\nu'$, whereas the reducible particle-particle channel has its main contribution along the secondary diagonal $\nu=-\nu'-\omega$, shifted by a constant ω.

3.1.4 $\Gamma_{d(ensity)}$ and $\Gamma_{m(agnetic)}$

Now we have all ingredients for calculating the asymptotics of the spin-diagonalized vertices Γ_d and Γ_m, defined as

$$\Gamma_{d,asympt} = \Gamma_{\uparrow\uparrow} + \Gamma_{\uparrow\downarrow} \tag{48}$$

$$\Gamma_{m,asympt} = \Gamma_{\uparrow\uparrow} - \Gamma_{\uparrow\downarrow}. \tag{49}$$

Inserting the results derived above, we end up with an equation for the asymptotic behavior of Γ_d and Γ_m (Eq. 50,51).

$$\begin{aligned}\Gamma_{d,asympt} = U + \frac{U^2}{\beta^2}\sum_{\nu_1\nu_2}[2\chi_{\uparrow\uparrow}^{\nu_1\nu_2(\nu'-\nu)} - \chi_{\uparrow\downarrow}^{\nu_1\nu_2(\nu'-\nu)} - (\chi_{\uparrow\downarrow}^{\nu_1\nu_2(-\nu_1-\nu_2+\nu+\nu'+\omega)} \\ + \beta G(\nu_1)G(-\nu_1+\nu+\nu'+\omega)\delta_{(-\nu_1-\nu_2+\nu+\nu'+\omega)0})]\end{aligned} \tag{50}$$

$$\begin{aligned}\Gamma_{m,asympt} = -U + \frac{U^2}{\beta^2}\sum_{\nu_1\nu_2}[\chi_{\uparrow\downarrow}^{\nu_1\nu_2(\nu'-\nu)} + \chi_{\uparrow\downarrow}^{\nu_1\nu_2(-\nu_1-\nu_2+\nu+\nu'+\omega)} \\ + \beta G(\nu_1)G(-\nu_1+\nu+\nu'+\omega)\delta_{(-\nu_1-\nu_2+\nu+\nu'+\omega)0}]\end{aligned} \tag{51}$$

3.2 Particle-Particle channel

In the previous section, we calculated the asymptotics of the longitudinal irreducible particle-hole channel Γ_{ph}. Due to the crossing symmetry, we do not have to calculate $\Gamma_{\overline{ph}}$ explicitly and therefore, we will now turn to the last remaining channel - the particle-particle irreducible channel Γ_{pp}. The natural frequency notation for this channel is the particle-particle notation (see Eq. 13) and, therefore, Λ_{asympt}, $\Phi_{ph,asympt}$ and $\Phi_{\overline{ph},asympt}$ are also calculated adopting this frequency convention. Although it is possible to calculate $\Phi_{ph,asympt}$ and use the crossing symmetry to get $\Phi_{\overline{ph},asympt}$, we will explicitly calculate both parts to get a clear understanding of all contributions to $\Gamma_{pp,asympt}$. To avoid any confusion concerning the frequency notation, we will denote the frequency notation with an "pp" superscript.

3.2.1 fully irreducible diagrams Λ

Since the Pauli principle has to be fulfilled no matter which frequency notation we adopt, we can directly use our results from the irreducible particle-hole channel for Λ.

($\uparrow\uparrow$)

For $\sigma = \sigma'$ the diagram Fig. 22, which corresponds to an instantaneous and local interaction of two up-spin electrons, vanishes due to Pauli's principle. All higher-order contributions to $\Lambda_{\uparrow\uparrow}$ are at least of the order $O(\frac{1}{\nu})$, and hence, do not contribute to the asymptotics, as it was already discussed for the longitudinal particle-hole channel.

($\uparrow\downarrow$)

For ($\uparrow\downarrow$), the contribution of the lowest order diagram reads as

$$\Lambda_{asympt,\uparrow\downarrow} = +U. \tag{52}$$

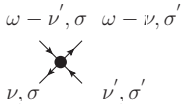

Figure 22: Fully irreducible first order diagram. Due to Pauli's principle, this diagram vanishes for $\sigma = \sigma^{'}$

3.2.2 reducible particle-hole diagrams $\Phi_{ph,asympt}$

$(\uparrow\uparrow)$

The lowest order diagram is the second order bubble diagram in Fig. 23 In

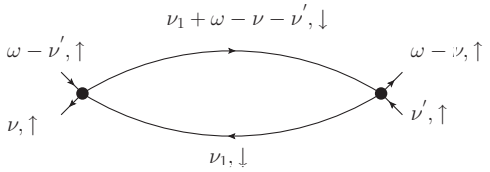

Figure 23: Particle-hole reducible second order diagram for $(\uparrow\uparrow)$

terms of Green's functions, it has the following form (Eq. 53)

$$P_7(\nu,\nu^{'},\omega) = +\frac{U^2}{\beta}\sum_{\nu_1} G(\nu_1)G(\nu_1+\omega-\nu-\nu^{'}). \tag{53}$$

Looking at the second Green's function $G(\nu_1+\omega-\nu-\nu^{'})$ in Eq. 53, we find that this diagram depends on $\omega-\nu-\nu^{'}$ only and contributes to the asymptotics for

$$\omega-\nu-\nu^{'} = const \tag{54}$$

assuming a maximum for

$$\omega-\nu-\nu^{'} = 0. \tag{55}$$

Considering higher order terms (Fig. 24,25), we find a general expression for such contributions according to Fig. 25.

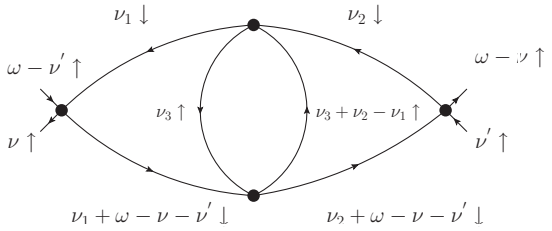

Figure 24: 4th order longitudinal particle-hole reducible diagram in particle-particle frequency notation

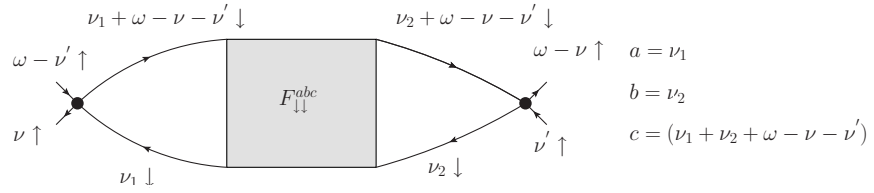

Figure 25: General longitudinal particle-hole reducible diagram in particle-particle frequency notation with vertex insertions

$$P_8(\nu,\nu',\omega) = +\frac{U^2}{\beta^2}\sum_{\nu_1\nu_2} G(\nu_1)G(\nu_2)F^{pp,\nu_1\nu_2(\nu_1+\nu_2+\omega-\nu-\nu')}_{\downarrow\downarrow} \\ G(\nu_1+\omega-\nu-\nu')G(\nu_2+\omega-\nu-\nu'). \tag{56}$$

($\uparrow\downarrow$)

For the ($\uparrow\downarrow$)-case, the lowest order longitudinal particle-hole reducible diagram which does not vanish is the third order diagram Fig. 26. In contrast to the

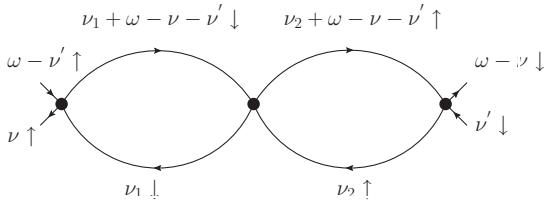

Figure 26: Particle-hole reducible third order diagram in particle-particle notation

second order bubble Fig. 23, which is not part of the diagram with general vertex insertions Fig. 25 and therefore, has to be considered separately when summing up all contributions, the third order diagram is part of the general longitudinal particle-hole reducible diagram in Fig. 27. Therefore, the analytic expression for $\Phi^{pp}_{ph\uparrow\downarrow,asympt}$ according to Fig. 27 reads as

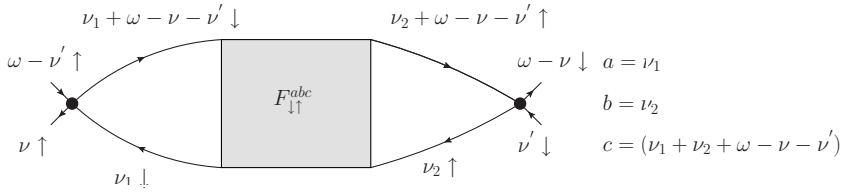

Figure 27: Particle-hole reducible diagram in particle-particle notation with general vertex insertions

$$P_9(\nu,\nu',\omega) = +\frac{U^2}{\beta^2}\sum_{\nu_1\nu_2} G(\nu_1)G(\nu_2)F^{pp,\nu_1\nu_2(\nu_1+\nu_2+\omega-\nu-\nu')}_{\downarrow\uparrow} \\ G(\nu_1+\omega-\nu-\nu')G(\nu_2+\omega-\nu-\nu'). \tag{57}$$

Summing up all contributions to $\Phi_{ph}^{pp\,2}$ leads to

$$\Phi^{pp}_{ph\uparrow\uparrow,asympt} = +\frac{U^2}{\beta^2}\sum_{\nu_1\nu_2}[\beta G(\nu_1)G(\nu_1+\omega-\nu-\nu^{'})\delta_{\nu_1\nu_2} + G(\nu_1)G(\nu_2)F^{pp,\nu_1\nu_2(\nu_1+\nu_2+\omega-\nu-\nu^{'})}_{\downarrow\downarrow}G(\nu_1+\omega-\nu-\nu^{'})G(\nu_2+\omega-\nu-\nu^{'})] \tag{58}$$

$$\Phi^{pp}_{ph\uparrow\downarrow,asympt} = +\frac{U^2}{\beta^2}\sum_{\nu_1\nu_2} G(\nu_1)G(\nu_2)F^{pp,\nu_1\nu_2(\nu_1+\nu_2+\omega-\nu-\nu^{'})}_{\downarrow\uparrow} G(\nu_1+\omega-\nu-\nu^{'})G(\nu_2+\omega-\nu-\nu^{'}). \tag{59}$$

We want to express $\Phi^{pp}_{ph\uparrow\uparrow,asympt}$ and $\Phi^{pp}_{ph\uparrow\downarrow,asympt}$ in terms of χ, which leads to

$$+\frac{U^2}{\beta^2}\sum_{\nu_1\nu_2}\beta G(\nu_1)G(\nu_1+\omega-\nu-\nu^{'})\delta_{\nu_1\nu_2} = -\frac{U^2}{\beta^2}\sum_{\nu_1\nu_2}\chi_0^{pp,\nu_1\nu_2(\nu_1+\nu_2+\omega-\nu-\nu^{'})} \tag{60}$$

$$+\frac{U^2}{\beta^2}\sum_{\nu_1\nu_2}G(\nu_1)G(\nu_2)F^{pp,\nu_1\nu_2(\nu_1+\nu_2+\omega-\nu-\nu^{'})}_{\downarrow\downarrow}G(\nu_1+\omega-\nu-\nu^{'})G(\nu_2+\omega-\nu-\nu^{'}) = \frac{U^2}{\beta^2}\sum_{\nu_1\nu_2}[-\chi^{pp,\nu_1\nu_2(\nu_1+\nu_2+\omega-\nu-\nu^{'})}_{\uparrow\uparrow} + \chi_0^{pp,\nu_1\nu_2(\nu_1+\nu_2+\omega-\nu-\nu^{'})}] \tag{61}$$

$$+\frac{U^2}{\beta^2}\sum_{\nu_1\nu_2}G(\nu_1)G(\nu_2)F^{pp,\nu_1\nu_2(\nu_1+\nu_2+\omega-\nu-\nu^{'})}_{\downarrow\uparrow}G(\nu_1+\omega-\nu-\nu^{'})G(\nu_2+\omega-\nu-\nu^{'}) = \frac{U^2}{\beta^2}\sum_{\nu_1\nu_2}-\chi^{pp,\nu_1\nu_2(\nu_1+\nu_2+\omega-\nu-\nu^{'})}_{\downarrow\uparrow} \tag{62}$$

Inserting Eq. 60 and Eq. 61 into Eq. 58 leads to

$$\Phi^{pp}_{ph\uparrow\uparrow,asympt} = +\frac{U^2}{\beta^2}\sum_{\nu_1\nu_2}-\chi^{pp,\nu_1\nu_2(\nu_1+\nu_2+\omega-\nu-\nu^{'})}_{\uparrow\uparrow} \tag{63}$$

and insterting Eq. 62 into Eq. 59 finally leads to

$$\Phi^{pp}_{ph\uparrow\downarrow,asympt} = -\frac{U^2}{\beta^2}\sum_{\nu_1\nu_2}\chi^{pp,\nu_1\nu_2(\nu_1+\nu_2+\omega-\nu-\nu^{'})}_{\downarrow\uparrow}. \tag{64}$$

3.2.3 reducible vertical particle-hole diagrams $\Phi^{pp}_{\overline{ph}}$

For the reducible vertical particle-hole diagrams $\Phi^{pp}_{\overline{ph},asympt}$, we can directly use our results for $\Phi_{\overline{ph},asympt}$ in particle-hole notation. In fact as we see in Eq. 14,

[2]To avoid any confusion concerning the frequency notation, we will denote the particle-particle frequency notation with an "pp" superscript

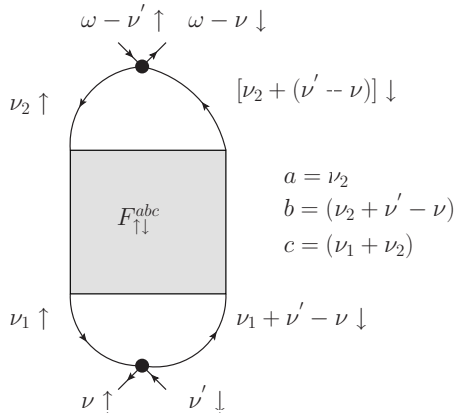

Figure 28: General vertical particle-hole reducible diagram in particle-particle frequency notation with vertex insertions

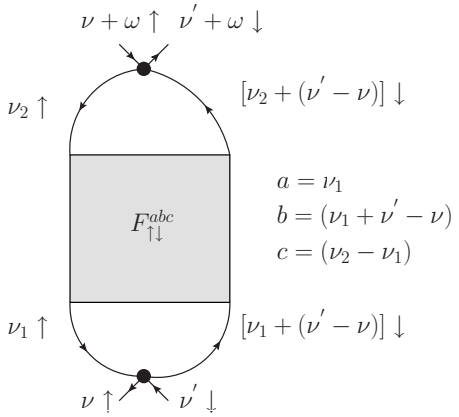

Figure 29: General vertical particle-hole reducible diagram in particle-hole frequency notation with vertex insertions

the two frequency notations can be transformed into each other by substituting ω as

$$\omega \to \omega - \nu - \nu'. \tag{65}$$

Since the transformation only affects ω, $\Phi_{\overline{ph},asympt}$ is completely not affected by this transformation. To illustrate this, we show a diagram contributing to $\Phi_{\overline{ph},asympt}$ in particle-particle notation and compare it to its counterpart in the particle-hole notation. In terms of Green's functions, Fig. 28 can be written as

$$P_{10}(\nu,\nu') = +\frac{U^2}{\beta^2}\sum_{\nu_1\nu_2} G(\nu_1)G(\nu_2)F^{pp,\nu_1(\nu_1+\nu'-\nu)(\nu_1+\nu_2)}_{\uparrow\downarrow} G(\nu_1+\nu'-\nu)G(\nu_2+\nu'-\nu). \tag{66}$$

whereas for the particle-hole notation, Fig. 29 can be written as

$$P_{11}(\nu,\nu') = +\frac{U^2}{\beta^2}\sum_{\nu_1\nu_2} G(\nu_1)G(\nu_2)F^{\nu_1(\nu_1+\nu'-\nu)(\nu_2-\nu_1)}_{\uparrow\downarrow} G(\nu_1+\nu'-\nu)G(\nu_2+\nu'-\nu). \tag{67}$$

Both diagrams do not depend on ω and we are summing over all internal frequencies (ν_1, ν_2), which leads to the same result for both equations. This can also be seen by rewriting $F^{pp,\nu_1(\nu_1+\nu'-\nu)(\nu_1+\nu_2)}_{\uparrow\downarrow}$ in Eq. 66 in terms of the ph-notation. According to Eq. 68

$$F^{pp,\nu\nu'\omega}_{\uparrow\downarrow} = F^{\nu\nu'(\omega-\nu-\nu')}_{\uparrow\downarrow} \tag{68}$$

the vertex function in Eq. 67 can be written as

$$F^{pp,\nu_1(\nu_1+\nu'-\nu)(\nu_1+\nu_2)}_{\uparrow\downarrow} = F^{\nu_1(\nu_1+\nu'-\nu)(\nu_2-\nu_1)}_{\uparrow\downarrow} \tag{69}$$

Since this ω-independency is valid for all asymptotic $\Phi_{\overline{ph}}$ diagrams, we do not have to calculate $\Phi_{\overline{ph}}$ again for the irreducible particle-particle channel, because it is the same as for the longitudinal particle-hole channel.

3.2.4 $\Gamma_{s(inglet)}$ and $\Gamma_{t(riplet)}$

Now we have all ingredients for calculating $\Gamma_{s(inglet)}$ and $\Gamma_{t(riplet)}$. We use the spin-diagonalized basis, derived in Sec. 2.2 and sum up all relevant contributions

$$\Gamma_{t(riplet)asympt} = \Gamma_{\uparrow\uparrow} \tag{70}$$

$$\Gamma_{s(inglet)asympt} = 2\Gamma_{\uparrow\downarrow} - \Gamma_{\uparrow\uparrow} = 2\Gamma_{\uparrow\downarrow} - \Gamma_t. \tag{71}$$

Inserting all contributions lead to

$$\begin{aligned}\Gamma_t &= \Phi^{pp}_{asympt,ph\uparrow\uparrow} + \Phi_{asympt,\overline{ph}\uparrow\uparrow} \\ &= -\frac{U^2}{\beta^2}\sum_{\nu_1\nu_2}[\chi^{pp,\nu_1\nu_2(\nu_1+\nu_2+\omega-\nu-\nu')}_{\uparrow\uparrow} + \chi^{\nu_2\nu_1(\nu'-\nu)}_{\uparrow\uparrow}]\end{aligned} \tag{72}$$

$$\begin{aligned}\Gamma_s &= 2(\Lambda + \Phi^{pp}_{asympt,ph\uparrow\downarrow} + \Phi_{asympt,\overline{ph}\uparrow\downarrow}) - \Phi^{pp}_{asympt,ph\uparrow\uparrow} - \Phi_{asympt,\overline{ph}\uparrow\uparrow} \\ &= 2U - 2\frac{U^2}{\beta^2}\sum_{\nu_1\nu_2}(\chi^{pp,\nu_1\nu_2(\nu_1+\nu_2+\omega-\nu-\nu')}_{\uparrow\downarrow} - \chi^{\nu_1\nu_2(\nu'-\nu)}_{\uparrow\uparrow} + \chi^{\nu_1\nu_2(\nu'-\nu)}_{\uparrow\downarrow}) - \Gamma_t\end{aligned} \tag{73}$$

Although we are now able to calculate the asymptotic triplet and singlet channel numerically, we have a rather inconvenient form of Eq. 72 and Eq. 73, since we are mixing two different frequency notations in one equation. It is advantageous to perform the frequency summation in only one notation and choose the particle hole notation for this. We therefore want to express $\chi^{pp,\nu_1\nu_2(\nu_1+\nu_2+\omega-\nu-\nu')}_{\uparrow\downarrow}$ and $\chi^{pp,\nu_1\nu_2(\nu_1+\nu_2+\omega-\nu-\nu')}_{\uparrow\uparrow}$ in the particle-hole notation which lead to

$$\chi^{pp,\nu_1\nu_2(\nu_1+\nu_2+\omega-\nu-\nu')}_{\uparrow\uparrow} \overset{\omega\to\omega-\nu_1-\nu_2}{=} \chi^{\nu_1\nu_2(\omega-\nu-\nu')}_{\uparrow\uparrow} \tag{74}$$

$$\chi^{pp,\nu_1\nu_2(\nu_1+\nu_2+\omega-\nu-\nu')}_{\uparrow\downarrow} \overset{\omega\to\omega-\nu_1-\nu_2}{=} \chi^{\nu_1\nu_2(\omega-\nu-\nu')}_{\uparrow\downarrow} \tag{75}$$

Eq. 72 and Eq. 73 can now be written as

$$\Gamma_t = -\frac{U^2}{\beta^2}\sum_{\nu_1\nu_2}[\chi^{\nu_1\nu_2(\omega-\nu-\nu')}_{\uparrow\uparrow} + \chi^{\nu_2\nu_1(\nu'-\nu)}_{\uparrow\uparrow}] \tag{76}$$

$$\Gamma_s = 2U - 2\frac{U^2}{\beta^2}\sum_{\nu_1\nu_2}(\chi^{\nu_1\nu_2(\omega-\nu-\nu')}_{\uparrow\downarrow} - \chi^{\nu_1\nu_2(\nu'-\nu)}_{\uparrow\uparrow} + \chi^{\nu_1\nu_2(\nu'-\nu)}_{\uparrow\downarrow}) - \Gamma_t, \tag{77}$$

which allows for numerical calculation in ph notation only.

3.3 Numerical calculation of the asymptotic Γ_{asympt} using exact diagonalization

In the previous sections, we derived equations for $\Gamma_{dmst,asympt}$ in terms of generalized susceptibilities $\chi^{\nu\nu'\omega}_{\sigma\sigma'}$. We have shown that for $\Gamma_{dmst,asympt}$ we only

have to deal with effective one-particle functions instead of the general three-frequency function $\chi_{\sigma\sigma'}^{\nu\nu'\omega}$. We will explicitly discuss this one-frequency dependence by using the definition of $\chi_{\sigma\sigma'}^{\nu\nu'\omega}$ (Eq. 12 for the ph and Eq. 13 for pp notation). The last step will be the numerical calculation of $\Gamma_{dmst,asympt}$ employing a standard ED (exact diagonalization) program. We will now calculate each part of Γ_{dmst} (Eq. 50, 51, 76, 77) separately.

3.3.1 Explicit calculation of $\sum_{\nu_1\nu_2} \chi_{\sigma\sigma'}^{\nu_1\nu_2(\nu'-\nu)}$

Inserting the definition of $\chi_{\sigma\sigma'}^{\nu\nu'\omega}$ (Eq. 12) leads to

$$\begin{aligned}\sum_{\nu_1\nu_2} \chi_{\sigma\sigma'}^{\nu_1\nu_2(\nu'-\nu)} = &\sum_{\nu_1\nu_2} \int_0^\beta d\tau_1 d\tau_2 d\tau_3 e^{-i\nu_1(\tau_1-\tau_2)} \\ &e^{-i\nu_2\tau_3} e^{i(\nu-\nu')\tau_2} e^{-i(\nu'-\nu)\tau_3} \chi_{\sigma\sigma'}(\tau_1,\tau_2,\tau_3)\end{aligned} \tag{78}$$

with

$$\begin{aligned}\chi_{\sigma\sigma'}(\tau_1\tau_2\tau_3) :=& < T(\hat{c}_\sigma^\dagger(\tau_1)\hat{c}_\sigma(\tau_2)\hat{c}_{\sigma'}^\dagger(\tau_3)\hat{c}_{\sigma'}) > \\ &- < T(\hat{c}_\sigma^\dagger(\tau_1)\hat{c}_\sigma(\tau_2)) >< T(\hat{c}_{\sigma'}^\dagger(\tau_3)\hat{c}_{\sigma'}) > .\end{aligned} \tag{79}$$

We can now interchange the summation and integration and use the following identity for summation over Matsubara frequencies:

$$\sum_\nu e^{-i\nu\tau} = \beta\delta(\tau). \tag{80}$$

Inserting Eq. 80 into Eq. 78 and performing the summations over ν_1 and ν_2 we get

$$\sum_{\nu_1\nu_2} \chi_{\sigma\sigma'}^{\nu_1\nu_2(\nu'-\nu)} = \beta^2 \int_0^\beta d\tau e^{i(\nu'-\nu)} \chi_{\sigma\sigma'}(\tau,\tau,0) \tag{81}$$

where $\tau_1 \to \tau$, $\tau_1 = \tau_2$ and $\tau_3 = 0$. Now there is only one time-integration left with a bosonic frequency $(\nu' - \nu)$ in the exponential. Since in this work, we will calculate Eq. 81 numerically employing a ED solver, we have to introduce a representation in terms of of the matrix elements of $\chi_{\sigma\sigma'}(\tau,\tau,0)$ which is known as Lehmann-Representation [45]. It is the representation of correlation functions of a many-body problems in terms of a complete set $\{|n>\}$ of eigenstates of the full many-particle Hamiltonian. Since $\chi_{\sigma\sigma'}(\tau,\tau,0)$ contains a matrix element of a two-particle propagator and a product of two one-particle propagators, we will discuss them separately. We start with the matrix element of the two-particle propagator, which we call A

$$A = < T(\hat{c}_\sigma^\dagger(\tau)\hat{c}_\sigma(\tau)\hat{c}_{\sigma'}^\dagger\hat{c}_{\sigma'}) > \tag{82}$$

Since the integration in Eq. 81 is on the positive time-interval $[0,\beta]$, the operators are already arranged in the correct time-order. In the next step, we insert

a complete set of eigenstates $\{|n>\}$ of the full Hamiltonian and use the finite temperature expression of the expectation value $< ... >$

$$A = \frac{1}{Z}\sum_{i,n} < i|e^{-\beta H}(\hat{c}_\sigma(\tau)^\dagger \hat{c}_\sigma(\tau)|n >< n|\hat{c}^\dagger_{\sigma'}\hat{c}_{\sigma'})|i > \tag{83}$$

inserting the Heisenberg picture of the operators $\hat{c}$ and $\hat{c}^\dagger$ leads to

$$A = \frac{1}{Z}\sum_{i,n} e^{-\beta E_i}e^{-E_i\tau}e^{-E_n\tau} < i|\hat{c}^\dagger_\sigma\hat{c}_\sigma|n >< n|\hat{c}^\dagger_{\sigma'}\hat{c}_{\sigma'}|i > . \tag{84}$$

We now insert Eq. 84 into Eq. 81 and integrate over $[0,\beta]$ For $(\nu^{'} \neq \nu)$ and $E_i \neq E_n$, the integration is straightforward and lead to

$$\beta^2\int_0^\beta d\tau e^{i(\nu^{'}-\nu)}A = \frac{\beta^2}{Z}\sum_{i,n} < i|(\hat{c}^\dagger_\sigma\hat{c}_\sigma|n >< n|\hat{c}^\dagger_{\sigma'}\hat{c}_{\sigma'})|i > \frac{(e^{-E_n\beta}-e^{-E_i\beta})}{i(\nu'-\nu)+E_i-E_n} \tag{85}$$

We note that Eq. 85 contains singularities within the integration interval. At the pole $(\nu^{'} = \nu \wedge E_i = E_n)$ however these can be easily resolved by means of the L'Hospital rule:

$$\beta^2\int_0^\beta d\tau e^{i(\nu^{'}-\nu)}A \overset{\substack{\nu\to\nu^{'}\\ E_i=E_n}}{=} \frac{\beta^3}{Z}\sum_{i,n} < i|(\hat{c}^\dagger_\sigma\hat{c}_\sigma|n >< n|\hat{c}^\dagger_{\sigma'}\hat{c}_{\sigma'})|i > e^{-E_n\beta} \tag{86}$$

We now discuss the second part of $\chi_{\sigma\sigma'}(\tau,\tau,0)$, which we call B

$$B =< \hat{c}^\dagger_\sigma(\tau)\hat{c}_\sigma(\tau) >< \hat{c}^\dagger_{\sigma'}\hat{c}_{\sigma'} > \tag{87}$$

The evaluation of B is much simpler since we do not have to insert a complete basis set and therefore can directly express Eq. 88 as

$$B = \frac{1}{Z^2}\sum_{i,j} < i|e^{-\beta H}\hat{c}_\sigma(\tau)^\dagger\hat{c}_\sigma(\tau)|i >< j|e^{-\beta H}\hat{c}^\dagger_{\sigma'}\hat{c}_{\sigma'}|j > \tag{88}$$

which then gives

$$B = \frac{1}{Z^2}\sum_{i,j} e^{-\beta E_i}e^{-\beta E_j} < i|\hat{c}^\dagger_\sigma\hat{c}_\sigma|i >< j|\hat{c}^\dagger_{\sigma'}\hat{c}_{\sigma'}|j > \tag{89}$$

. We now insert Eq. 89 again into Eq. 81 and integrate over $[0,\beta]$

$$\begin{aligned}\beta^2\int_0^\beta d\tau e^{i(\nu^{'}-\nu)}B =& \frac{\beta^2}{Z^2}\frac{1}{i(\nu'-\nu)}(e^{i(\nu^{'}-\nu)\beta}-1)\\ & \sum_{i,j} e^{-\beta E_i}e^{-\beta E_j} < i|\hat{c}^\dagger_\sigma\hat{c}_\sigma|i >< j|\hat{c}^\dagger_{\sigma'}\hat{c}_{\sigma'}|j >\end{aligned} \tag{90}$$

For $\nu^{'} \neq \nu$ Eq. 90 gives 0 since

$$e^{i(\nu^{'}-\nu)\beta} - 1 = e^{i\frac{2n\pi}{\beta}\beta} - 1 = 0. \tag{91}$$

For $\nu^{'} = \nu$ the integration is trivial and leads to

$$\beta^2 \int_0^\beta d\tau B = \frac{\beta^3}{Z^2} \sum_{i,j} e^{-\beta E_i} e^{-\beta E_j} < i|(\hat{c}_\sigma^\dagger \hat{c}_\sigma|i >< j|\hat{c}_{\sigma'}^\dagger \hat{c}_{\sigma'})|j > \tag{92}$$

Eq. 85, Eq. 86 and Eq. 90, Eq. 92 are now the expectation values which we can easily be evaluated by using an ED-solver. In fact, contrary to the general case of a two-particle Green's function, here we have only matrix elements of density operators, which allows for significant speed-up when using the ED-solver.

3.3.2 Explicit calculation of $\sum_{\nu_1\nu_2} \chi_{\uparrow\downarrow}^{\nu_1\nu_2(-\nu_1-\nu_2+\nu+\nu^{'}+\omega)}$

Inserting the definition of $\chi_{\sigma\sigma'}^{\nu\nu^{'}\omega}$ (Eq. 12) leads to

$$\begin{aligned}\sum_{\nu_1\nu_2} \chi_{\uparrow\downarrow}^{\nu_1\nu_2(-\nu_1-\nu_2+\nu+\nu^{'}+\omega)} = \sum_{\nu_1\nu_2} \int_0^\beta d\tau_1 d\tau_2 d\tau_3 e^{-i\nu_1\tau_1} e^{i(-\nu_2+\nu+\nu^{'}+\omega)\tau_2} \\ e^{-i(\nu_1+\nu+\nu^{'}+\omega)\tau_3} \chi_{\uparrow\downarrow}(\tau_1,\tau_2,\tau_3)\end{aligned} \tag{93}$$

with

$$\begin{aligned}\chi_{\uparrow\downarrow}(\tau_1\tau_2\tau_3) :=& < T(\hat{c}_\uparrow^\dagger(\tau_1)\hat{c}_\uparrow(\tau_2)\hat{c}_\downarrow^\dagger(\tau_3)\hat{c}_\downarrow) > \\ &- < T(\hat{c}_\uparrow^\dagger(\tau_1)\hat{c}_\uparrow(\tau_2)) >< T(\hat{c}_\downarrow^\dagger(\tau_3)\hat{c}_\downarrow) > .\end{aligned} \tag{94}$$

For the first part of Eq. 93, we can rewrite the exponential functions and use the identity Eq. 80 for summation over Matsubara frequencies.

$$\begin{aligned}A :=& \sum_{\nu_1\nu_2} \int_0^\beta d\tau_1 d\tau_2 d\tau_3 e^{-i\nu_1\tau_1} e^{i(-\nu_2+\nu+\nu^{'}+\omega)\tau_2} e^{-i(\nu_1+\nu+\nu^{'}+\omega)\tau_3} < ... > \\ =& \int_0^\beta d\tau_1 d\tau_2 d\tau_3 (\sum_{\nu_1} e^{-i\nu_1(\tau_1-\tau_3)})(\sum_{\nu_2} e^{-i\nu_2\tau_2}) \times e^{i(\nu+\nu^{'}+\omega)(\tau_2-\tau_3)} < ... > \\ \overset{Eq.(80)}{=}& \beta^2 \int_0^\beta d\tau e^{-i\tau(\nu+\nu^{'}+\omega)} < T(\hat{c}_\uparrow^\dagger(\tau)\hat{c}_\uparrow(0)\hat{c}_\downarrow^\dagger(\tau)\hat{c}_\downarrow(0)) >\end{aligned} \tag{95}$$

For the second part of Eq. 93, due to the periodicity of the Matsubara Green's function, we can perform the transformation $\tau_1 \rightarrow \tau_1 + \tau_2$[3].

$$\begin{aligned}B :=& -\sum_{\nu_1\nu_2} \int_0^\beta d\tau_1 d\tau_2 d\tau_3 e^{-i\nu_1\tau_1} e^{i(-\nu_2+\nu+\nu^{'}+\omega)\tau_2} e^{-i(\nu_1+\nu+\nu^{'}+\omega)\tau_3} < .. >< .. > \\ =& -\sum_{\nu_1\nu_2} \int_0^\beta d\tau_1 d\tau_3 e^{-i\nu\tau_1} e^{-i(-\nu_1+\nu+\nu^{'}+\omega)\tau_3} \times \left(\int_0^\beta d\tau_2 e^{i(-\nu_1-\nu_2+\nu+\nu^{'}+\omega)\tau_2} \right) < .. >< .. > .\end{aligned} \tag{96}$$

[3]This transformation does not affect the integration limits. For further details see Appendix of Ref. [40]

Performing the integration over τ_2 leads to

$$B = -\sum_{\nu_1\nu_2}\int_0^\beta d\tau_1 d\tau_2 d\tau_3 e^{-i\nu_1\tau_1} e^{i(-\nu_2+\nu+\nu^{'}+\omega)\tau_2} e^{-i(\nu_1+\nu+\nu^{'}+\omega)\tau_3} < .. >< .. >$$
$$= -\sum_{\nu_1\nu_2}\int_0^\beta d\tau_1 d\tau_3 e^{-i\nu\tau_1} e^{-i(-\nu_1+\nu+\nu^{'}+\omega)\tau_3} \times \left(\beta\delta_{(-\nu_1-\nu_2+\nu+\nu^{'}+\omega)0}\right) < .. >< .. > . \tag{97}$$

Since Eq. 97 cancels the last term of Eq. 50 and Eq. 51, we only have to calculate Eq. 95 explicitely.

We first perform the transformation $\tau \to \beta - \tau$ which leads to

$$A = \beta^2 \int_0^\beta d\tau e^{+i\tau(\nu+\nu^{'}+\omega)} < T(\hat{c}_\uparrow^\dagger(0)\hat{c}_\uparrow(\tau)\hat{c}_\downarrow^\dagger(0)\hat{c}_\downarrow(\tau)) > . \tag{98}$$

Applying the commutation rules for fermionic operators we get

$$A = -\beta^2 \int_0^\beta d\tau e^{+i\tau(\nu+\nu^{'}+\omega)} < T(\hat{c}_\uparrow(\tau)\hat{c}_\downarrow(\tau)\hat{c}_\uparrow^\dagger(0)\hat{c}_\downarrow^\dagger(0)) > . \tag{99}$$

Inserting a full basis set $\{|j><j|\}$ and using the definition of a finite temperature expectation value yields to the Lehmann-Representation of Eq. 100

$$A = -\frac{\beta^2}{Z}\sum_{i,j}\int_0^\beta d\tau e^{+i\tau(\nu+\nu^{'}+\omega)} < i|e^{-\beta H}\hat{c}_\uparrow(\tau)\hat{c}_\downarrow(\tau)|j >< j|\hat{c}_\uparrow^\dagger(0)\hat{c}_\downarrow^\dagger(0)|i > . \tag{100}$$

Since $\tau > 0$, the time ordering operator has no effect on the order of the operators and we can directly evaluate the matrix elements of Eq. (100)

$$A = -\frac{\beta^2}{Z}\sum_{i,j}\int_0^\beta d\tau e^{+i\tau(\nu+\nu^{'}+\omega)} e^{-\beta E_i} e^{\tau E_i} e^{-\tau E_j} < i|\hat{c}_\uparrow\hat{c}_\downarrow|j >< j|\hat{c}_\uparrow^\dagger\hat{c}_\downarrow^\dagger|i > . \tag{101}$$

Performing the time integration, we finally get

$$A = -\frac{\beta^2}{Z}\sum_{i,j}\frac{< i|\hat{c}_\uparrow\hat{c}_\downarrow|j >< j|\hat{c}_\uparrow^\dagger\hat{c}_\downarrow^\dagger|i >}{i(\nu+\nu^{'}+\omega)+E_i-E_j} \times \left(e^{-\beta E_j} - e^{-\beta E_i}\right). \tag{102}$$

As before, at the pole ($\nu+\nu^{'}+\omega = 0 \wedge E_i = E_j$), we have to apply L'Hospitals's rule which yields to

$$A \overset{\substack{\nu+\nu^{'}+\omega\to 0\\ E_i=E_j}}{=} -\frac{\beta^3}{Z}\sum_{i,j} < i|\hat{c}_\uparrow\hat{c}_\downarrow|j >< j|\hat{c}_\uparrow^\dagger\hat{c}_\downarrow^\dagger|i > \times e^{-\beta E_i}. \tag{103}$$

This way, Eq. 102 and Eq. 103 can now be solved by using a standard ED-Solver.

3.4 Downfolding procedure

Separation of low and high frequency parts of a given problem is common in theoretical physics. Also for some numerical solvers of DMFT (see Ref. [46]), such separation is used for the calculation of the self-energy: the numerical solution of the Dyson equation at low-frequencies is augmented by a high-frequency asymptotic expansion obtained from the lowest moments of the spectral function. As for the calculation of the irreducible vertex functions Γ, we can proceed in a similar way as in the DMFT-practice, but of course working at the level of the Bethe-Salpeter equation instead of the Dyson equation. We will now consider explicitly the Bethe-Salpeter equations for the four different channels (d,m,s,t) and use the high-frequency expansion in order to reduce the computational effort for the inversion of the equations. Following the derivation by Jan Kuneš [33], we will end up with an equation, where Γ can be obtained by inverting the Bethe-Salpeter equation truncated to the low-frequency regime plus a correction term including the high-frequency asymptotic Γ's.

We will write down a general Bethe-Salpeter equation for channels (d,m) in terms of matrices as following:

$$\underline{\underline{\chi}} = \underline{\underline{\chi_0}} - \frac{1}{\beta^2}\underline{\underline{\chi_0}} \times \underline{\underline{\Gamma}} \times \underline{\underline{\chi}} \tag{104}$$

The matrices $\underline{\underline{\chi}}$,$\underline{\underline{\chi_0}}$ and $\underline{\underline{\Gamma}}$ are arranged in sectors of small-$(\nu,\nu^{'})$ and large-$(\nu,\nu^{'})$ denoted by indices 0,1. E.g., the sector (0,1) of the matrix $\underline{\underline{\Gamma}}$ is a sector with small ν and large $\nu^{'}$ indices of $\Gamma^{\nu\nu^{'}\omega}$. For the moment, we do not specify how the border between the low and high frequency subspaces have to be chosen. This will be discussed in the next chapter. Using the above mentioned notation, equation Eq. (104) can be written as

$$\begin{bmatrix} A_{00} & A_{01} \\ A_{10} & A_{11} \end{bmatrix} = \begin{bmatrix} B_{00} & 0 \\ 0 & B_{11} \end{bmatrix} - \frac{1}{\beta^2} \begin{bmatrix} B_{00} & 0 \\ 0 & B_{11} \end{bmatrix} \begin{bmatrix} \Gamma_{00} & \Gamma_{01} \\ \Gamma_{10} & \Gamma_{11} \end{bmatrix} \begin{bmatrix} A_{00} & A_{01} \\ A_{10} & A_{11} \end{bmatrix} \tag{105}$$

where $A = \chi$ and $B = \chi_0$ for an easier reading. We now want to express Γ_{00} in terms of A_{00},B,Γ_{01},Γ_{10},Γ_{11} and we will use the results of the asymptotic of Γ for the latter three. Algebraic manipulations of equation Eq. (105) lead to

$$\Gamma_{00} = \beta^2 \left(\left[\Gamma_{01} A_{10} + \mathbb{1} \right] A_{00}^{-1} - B_{00}^{-1} \right) \tag{106}$$

with A_{10} being

$$A_{10} = -\frac{1}{\beta^2} \left(\mathbb{1} + \frac{1}{\beta^2} \Gamma_{11} \right)^{-1} \left(B_{11} \Gamma_{10} A_{00} \right). \tag{107}$$

Inserting Eq. (107) into Eq. (106) and switching to $\chi = A$ and $\chi_0 = B$ finally leads to

$$\Gamma_{00} = \beta^2 \left[\chi_{00}^{-1} - \chi_{0(00)}^{-1} - \frac{1}{\beta^2}\Gamma_{01} \left[\mathbb{1} + \frac{1}{\beta^2}\Gamma_{11} \right]^{-1} \chi_{0(11)}\Gamma_{10} \right]. \tag{108}$$

The last term of equation Eq.(108) can be interpreted as a correction to the inversion of the truncated Bethe-Salpeter equation in the low-frequency subspace ($\beta^2[\chi_{00}^{-1} - \chi_{0,00}^{-1}]$). For the remaining channels (s,t), we follow the same algebraic manipulation steps as for the (d,m) channels but now starting with a different Bethe-Salpeter equation. In fact, for the triplet channel, the Bethe-Salpeter equation can be written as

$$\underline{\underline{\chi^t_{pp}}} = \underline{\underline{\chi_{0,pp}}} - \frac{1}{2\beta^2} \left(\underline{\underline{\chi_{0,pp}}} + \underline{\underline{\chi_{pp}}} \right) \times \underline{\underline{\Gamma_{pp}}} \times \underline{\underline{\chi_{0,pp}}}. \tag{109}$$

If we now move to new variables $A = \chi_{pp} + \chi_{0,pp}$ and $B = \chi_{0,pp}$, Equation Eq. (109) can be written as

$$\underline{\underline{A}} = 2\underline{\underline{B}} - \frac{1}{2\beta^2} \underline{\underline{A}} \times \underline{\underline{\Gamma_{pp}}} \times \underline{\underline{B}}. \tag{110}$$

After algebraic manipulation of equation Eq. (110), we can again write down an equation for the low-frequency sector $\Gamma_{pp,00}$ as an inversion of a truncated Bethe-Salpeter equation plus a correction term

$$\Gamma^t_{pp,00} = 4\beta^2 A^{-1}_{00} - 2\beta^2 B^{-1}_{00} - \frac{1}{2\beta^2}\Gamma_{pp,01}B_{11} \left[\mathbb{1} + \frac{1}{2\beta^2}\Gamma_{pp,11}B_{11} \right]^{-1} \Gamma_{pp,10}. \tag{111}$$

For better reading, we have kept here the notation $A = (\chi_{pp} + \chi_{0,pp})$, $B = \chi_{0,pp}$.

The Bethe-Salpeter equation for the singlet channel can be written as

$$\underline{\underline{\chi^s_{pp}}} = -\underline{\underline{\chi_{0,pp}}} - \frac{1}{2\beta^2} \left(\underline{\underline{\chi_{0,pp}}} - \underline{\underline{\chi_{pp}}} \right) \times \underline{\underline{\Gamma_{pp}}} \times \underline{\underline{\chi_{0,pp}}}. \tag{112}$$

We will move to new variables $A = (\chi_{pp} - \chi_{0,pp})$ and $B = \chi_{0,pp}$ and write down equation Eq.(112) as

$$\underline{\underline{A}} = -2\underline{\underline{B}} + \frac{1}{2\beta^2} \underline{\underline{A}} \times \underline{\underline{\Gamma_{pp}}} \times \underline{\underline{B}}. \tag{113}$$

After algebraic manipulation of equation Eq. (113), we can again write down an equation for the low-frequency sector $\Gamma_{pp,00}$ as an inversion of a truncated Bethe-Salpeter equation plus a correction term

$$\Gamma^s_{pp,00} = 4\beta^2 A^{-1}_{00} + 2\beta^2 B^{-1}_{00} - \frac{1}{2\beta^2}\Gamma_{pp,01}B_{11} \left[\mathbb{1} - \frac{1}{2\beta^2}\Gamma_{pp,11}B_{11} \right]^{-1} \Gamma_{pp,10}. \tag{114}$$

These equation complete the analytical derivations we need to extend the work of Jan Kuneš [33] to the particle-particle channel as well as to the $\omega \neq 0$ case. As we will se by discussing our numerical results in the next chapter, the value of the (bosonic) transfer frequency ω plays an important role for a correct determination of a "low-frequency" subspace in actual calculations.

4 Numerical Results

In this chapter, the analytic expressions for $\Gamma_{dmst,asympt}$ derived in the previous chapter are exploited for a numerical determination of the DMFT vertex functions of the half filled Hubbard model, especially in the most interesting regime of the Mott-Hubbard Metal-to-Insulator transition (MIT). The chapter is divided into three parts. I will start with a short discussion of the Mott Metal-Insulator transition (MIT) and its influence on dynamical response functions. In the second part, numerical results for the vertex functions are presented and used to identify the hallmarks of the MIT within their frequency structures. In the last part, I will compare vertex functions, calculated via an inversion on a large frequency interval (320 fermionic frequencies), with the corresponding vertex functions, calculated by using only a small frequency interval (40-80 fermionic frequencies) plus a correction term, derived from the high-frequency asymptotic behavior. The results demonstrate the applicability of such procedure in all channels. Furthermore, comparing the numerically calculated vertex functions with the purely asymptotic high frequency vertex function has been helpful for determining the minimal frequency interval, required for numerical inversion

4.1 Physics of the Mott Metal-to-Insulator transition

The most important approach for describing the electronic properties of materials is based on electronic band theory. There exist numerous approximations, like the nearly free electron approximation or the tight binding model [47–49], which cover many aspects of the band structure of different materials. According to band theory, the electronic conductivity of materials is determined by the number of electrons per unit cell. If materials consist of a lattice of atoms, each with an outer shell of electrons which freely dissociate from their parent atoms and travel through the lattice, they are predicted as conductors by standard band theories. However, in 1937 de Boer and Verwey [50] pointed out that a variety of transition metal oxides, predicted to be conductors by band theory, are insulators. This problem had occurred because standard band theory treats the electron-electron interactions only rudimentarily, which is a good approximation for most of the metals but gets worse or even fails for a variety of other materials such as transition metal oxides. An explanation for this "anomaly" was first given by Nevill Mott and Rudolf Peierls [51]. They suggested that the electron-electron interaction (correlation effects) are the main reason for the metal to insulator transition within the transition metal oxides. Although the physical picture is very intuitive, non-perturbative and computational calculations of the correlation effects, and hence, of the metal-insulator transition (MIT) were not possible until the development of DMFT. Since a detailed explanation of the MIT can be found in the literature (e.g. [18,37,51]), we will concentrate here on the effects of the MIT on the vertex functions and susceptibilities.

4.2 Mott transition and Vertex Functions

4.2.1 The MIT in the susceptibilities

The MIT can be understood as the suppression of electron mobility in a partially filled system and the consequent formation of a long-living local moment due to correlation effects. At the one-particle level, the MIT is characterized by a divergence of the self energy $\Sigma(\omega)$ at $\omega = 0$, which suppresses the electronic spectral weight at the Fermi level while at the two-particle particle level, the MIT becomes manifest in the $\frac{1}{T}$ divergence of the local magnetic susceptibility $\chi_m(\omega = 0)$. In the SU(2)-symmetric case the magnetic susceptibility in $\tau-$space is given for $\tau > 0$ by

$$\chi_m(\tau) =< \hat{S}_z(\tau)\hat{S}_z > \tag{115}$$

with

$$\hat{S}_z(\tau) = \frac{1}{2}(\hat{n}_\uparrow(\tau) - \hat{n}_\downarrow(\tau)) \tag{116}$$

being the spin operator in z-direction. Hence, we can express $\chi_m(\tau)$ as

$$\chi_m(\tau) = \frac{1}{2}(< \hat{n}_\uparrow(\tau)\hat{n}_\uparrow > - < \hat{n}_\uparrow(\tau)\hat{n}_\downarrow >). \tag{117}$$

If we consider the regime of weak interactions ($U < U_{crit}$), where U_{crit} is the U at the Mott transition point, χ_m quickly decays in τ due to temporal fluctuations of the local spin due to the high electron mobility in the metallic regime, whereas in the limit of strong interaction ($U > U_{crit}$), all local spin correlations are strongly enhanced, resulting in a huge magnetic response function χ_m. In particular for $U > U_{crit}$ when the electron mobility is (almost totally) suppressed, $\chi_m(\tau)$ becomes an almost constant function in τ. In frequency space, this corresponds to a Curie-Weiss $\frac{1}{T}$ divergence of $\chi_m(\omega)$ at zero Matsubara frequency $\omega = 0$. In Fig. 30 and Fig. 31, we have plotted $\chi_d(\omega = 0)$, $\chi_m(\omega = 0)$ and $\chi_{pp}(\omega = 0)$ for $\beta = 26.0$ and $\beta = 50.0$ respectively. For both values of β, we observe a strong enhancement of $\chi_m(\omega = 0)$ at the MIT, reaching a plateau in the Mott insulating phase. However, this plateau is proportional to β, i.e. proportional to $\frac{1}{T}$. In contrast to $\beta = 50.0$, the behavior of $\chi_m(\omega = 0)$ is rather smooth for $\beta = 26.0$. This is consistent with the phase diagram of the Hubbard model, where at $T > T_c$ the MIT changes to a smooth crossover, while for $T < T_c$ we observe a first order phase transition. T_c is the lower tip of a crossover region where, in DMFT, a smooth and continuous change of the physical properties is found by increasing U. Note that this situation closely resembles the well-known one of the liquid-gas transition.

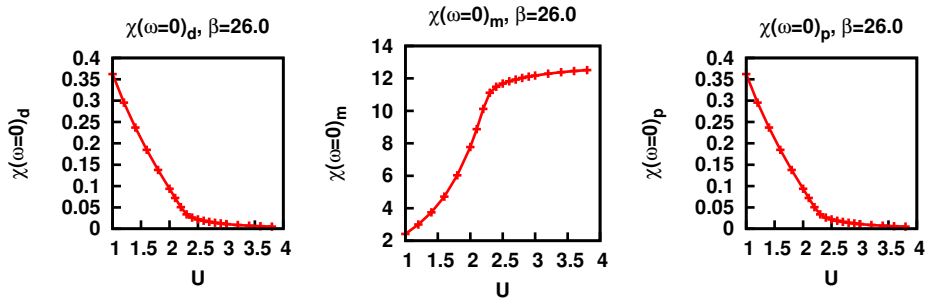

Figure 30: Visualization of the metal-insulator transition (MIT) in the two particle response functions $\chi_{d,m,pp}(\omega = 0)$ as function of U for $\beta = 26.0$.

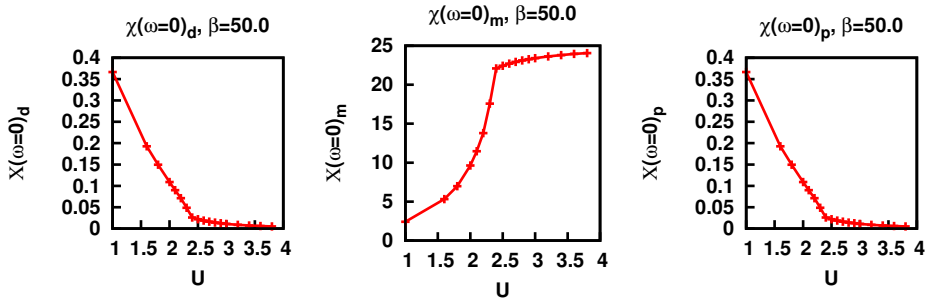

Figure 31: Same plot of the Metall-Insulator transition (MIT) in the two particle response functions $\chi_{d,m,pp}(\omega = 0)$ as function of U but now for $\beta = 50.0$. In comparison to $\beta = 26.0$ one observes a stronger divergence of the magnetic susceptibility due to the lower temperature compared to Fig. 30

While χ_m diverges at the MIT, local density and particle-particle fluctuations and hence, χ_d and χ_{pp} are strongly suppressed. The considerations are similar for both response functions, hence we will focus on χ_d only, which is given by

$$\chi_d(\tau) = 2(< \hat{n}_\uparrow(\tau)\hat{n}_\uparrow > + < \hat{n}_\uparrow(\tau)\hat{n}_\downarrow > -2 < \hat{n}_\uparrow(\tau) >< \hat{n}_\uparrow >). \qquad (118)$$

For $U < U_{crit}$ at $\tau = 0$, we observe a rather large value for $\chi_d(\tau = 0)$ due to a high electron mobility[4]. In the opposite limit, for $U > U_{crit}$ the onsite Coulomb repulsion is the dominating energy scale, thus suppressing, as we already mentioned, electron mobility. Hence, the local density response of the system on an additional chemical potential will become very small. As can be seen in Fig. 30 and Fig. 31, $\chi_d(\omega = 0)$ can be oughly estimated as $N(\epsilon = \epsilon_F) \approx \frac{1}{2}$ at $U = 0$ whereas for $U > U_{crit}$ we observe a smooth disappearance of χ_d for $T \gg T_{crit}$

[4]For $\tau = 0$ and $U = 0$ one can calculate Eq.118 analytically and gets $\chi_d(\tau = 0) = \frac{1}{2}$ for $U = 0$, while $\chi_d(\omega = 0) \approx N(\epsilon = \epsilon_F$

and a first order phase transition for $T \ll T_{crit}$.

As for the remaining susceptibility, χ_{pp}, one observes a very interesting phenomenon. χ_d and χ_{pp} perfectly coincide (Figs. 30, 31). This happens because, at half-filling, there exist an additional symmetry in the Hubbard model as well as in its associated AIM in DMFT called particle-hole symmetry. While for a detailed discussion we refer to the literature [40, 52], here we will give just a short explanation of this special symmetry:

At half filling, one can make use of a (partial) particle-hole transformation in order to map the repulsive ($U > 0$) onto the attractive ($U < 0$) Hubbard model [53]. By means of such a transformation the $x-$ and $y-$components of the Spin S are mapped on a local cooper-pair density ($c^\dagger_\uparrow c^\dagger_\downarrow$), which is connected to χ_{pp}, and its $z-$component to the charge density ($n_\uparrow$), which corresponds to χ_d [54]. For SU(2) symmetry, all three spin components are degenerate, which also holds for the quantities on which they are mapped. Hence, one gets the result, that local charge-fluctuations, referring to χ_d and local particle-fluctuations, referring to χ_{pp}, coincide, which is verified numerically in Figs. 30 and 31.

4.2.2 The MIT in the asymptotical irreducible vertex functions

In Chap. 3, we were able to express the asymptotics of the irreducible vertex functions Γ_{dmst} solely by using the physical susceptibilities $\chi_{m,d,pp}$. Hence one expects to observe hallmarks of the MIT also in the high-frequency behavior of these vertex functions. In fact, our calculations confirm this expectation. For instance, if we consider the asymptotics of, e.g., the irreducible vertex function Γ_d (see Eq. 50 in Chap. 3):

$$\begin{aligned}\Gamma_{d,asympt} = \; & U + \frac{U^2}{\beta^2}\sum_{\nu_1\nu_2}[2\chi^{\nu_1\nu_2(\nu'-\nu)}_{\uparrow\uparrow} - \chi^{\nu_1\nu_2(\nu'-\nu)}_{\uparrow\downarrow} - (\chi^{\nu_1\nu_2(-\nu_1-\nu_2+\nu+\nu'+\omega)}_{\uparrow\downarrow} \\ & + \beta G(\nu_1)G(-\nu_1+\nu+\nu'+\omega)\delta_{(-\nu_1-\nu_2+\nu+\nu'+\omega)0})] \\ = \; & U + 2U^2\chi_{\uparrow\uparrow}(\nu'-\nu) - U^2\chi_{\uparrow\downarrow}(\nu'-\nu) - U^2\chi_{pp}(\nu+\nu'+\omega),\end{aligned} \tag{119}$$

one can easily identify the main contributions alongside $\nu' - \nu = const$ and $\nu + \nu' + \omega = const$ assuming a maximum for $\nu' - \nu = 0$ and $\nu + \nu' + \omega = 0$. Considering Eq. 21 (Sec. 2.2), we are able to express the first two terms of the sum as linear combination of χ_d and χ_m

$$2\chi_{\uparrow\uparrow}(\nu-\nu') - \chi_{\uparrow\downarrow}(\nu-\nu') = \frac{3}{2}\chi_m(\nu-\nu') + \frac{1}{2}\chi_d(\nu-\nu'). \tag{120}$$

Hence, the enhancement of $\chi_m(0)$ at the MIT will be visible in the main diagonal ($\nu = \nu'$) of the vertex functions. This can be indeed observed in Fig. 32. The main diagonal (red colored), showing the contribution of Eq. 120 to Γ_d (Eq. 119) becomes actually strongly enhanced with increasing U (approaching the MIT).

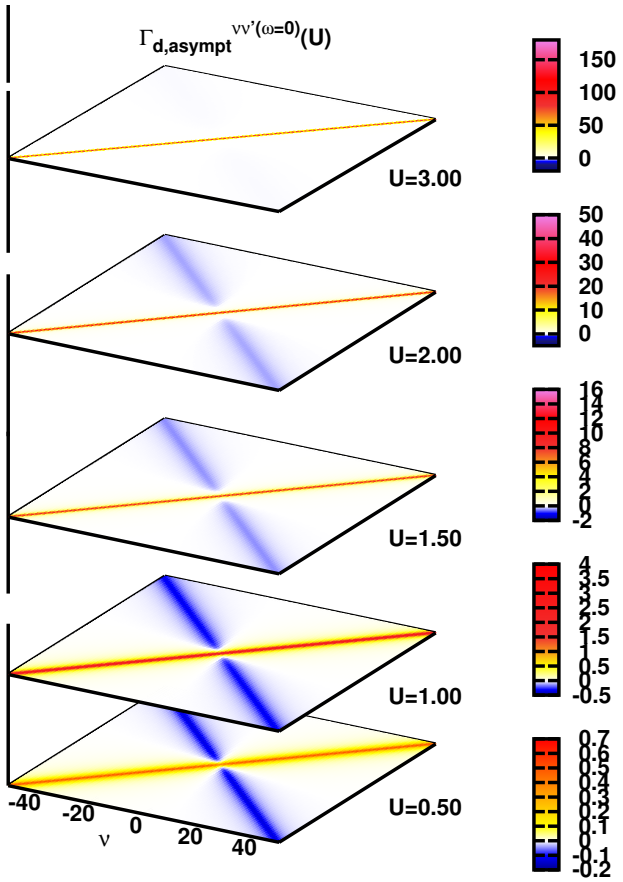

Figure 32: Layered density plot of $\Gamma_{d,asympt}^{\nu\nu'(\omega=0)}$ as function of ν, ν' for different U. Approaching the MIT leads to a strong enhancement of the main diagonal (red colored), which corresponds to a strong enhancement of the $\chi_m(0)$ contribution to $\Gamma_{d,asympt}$ in Eq. 119 (Note the changes in the color scale for increasing U.).

The evaluation of the sum over the last two terms of Eq. 119 leads to a expectation value

$$\int_0^\beta d\tau e^{i\omega\tau} < T(c_\uparrow(\tau)c_\downarrow(\tau)c_\downarrow^\dagger c_\uparrow^\dagger) >= \chi_{pp}(\omega), \tag{121}$$

which can be interpreted as a (local) cooper-pair response function and accounts for the secondary diagonal structure in Fig. 32. As one can observe, with increasing U, the secondary diagonal structure almost vanishes above the MIT ($U_{crit} \simeq 2.4$), indeed perfectly matching the behavior of the susceptibility $\chi_{pp}(\omega = 0)$ in Figs. 30 and 31. For the analysis of the asymptotics of the remaining irreducible vertex functions Γ_{mst}, we can proceed in a similar way as for Γ_d. One can see, for instance, for Γ_m

$$\begin{aligned}\Gamma_{m,asympt} = -U + \frac{U^2}{\beta^2}\sum_{\nu_1\nu_2}[&\chi_{\uparrow\downarrow}^{\nu_1\nu_2(\nu'-\nu)} + \chi_{\uparrow\downarrow}^{\nu_1\nu_2(-\nu_1-\nu_2+\nu+\nu'+\omega)} \\ &+ \beta G(\nu_1)G(-\nu_1+\nu+\nu'+\omega)\delta_{(-\nu_1-\nu_2+\nu+\nu'+\omega)0}],\end{aligned} \tag{122}$$

that the first term of the sum can be interpreted as linear combination of χ_d and χ_m as

$$\chi_{\uparrow\downarrow}(\nu - \nu^{'}) = \frac{1}{2}\chi_d(\nu - \nu^{'}) - \frac{1}{2}\chi_m(\nu - \nu^{'}). \tag{123}$$

It accounts for the main diagonal of Γ_m and diverges at $\nu = \nu^{'}$ due to the $(\frac{1}{T})$ divergence of $\chi_m(0)$ when approaching the MIT. As for Γ_d, the remaining terms of the sum in Eq. 122 are contributing to the secondary diagonal of Γ_m. In Fig. 33, one indeed observes a strong enhancement of the main diagonal (blue colored) with increasing U. As for Γ_d, the secondary diagonal almost vanishes above the MIT, which we have also found in χ_{pp} in Figs. 30 and 31. The main diagonal of Γ_d (Fig.32) and Γ_m (Fig.33) have opposite sign, which comes from the different sign, with which $\chi_m(\nu - \nu^{'})$ enters in Γ_d and Γ_m.

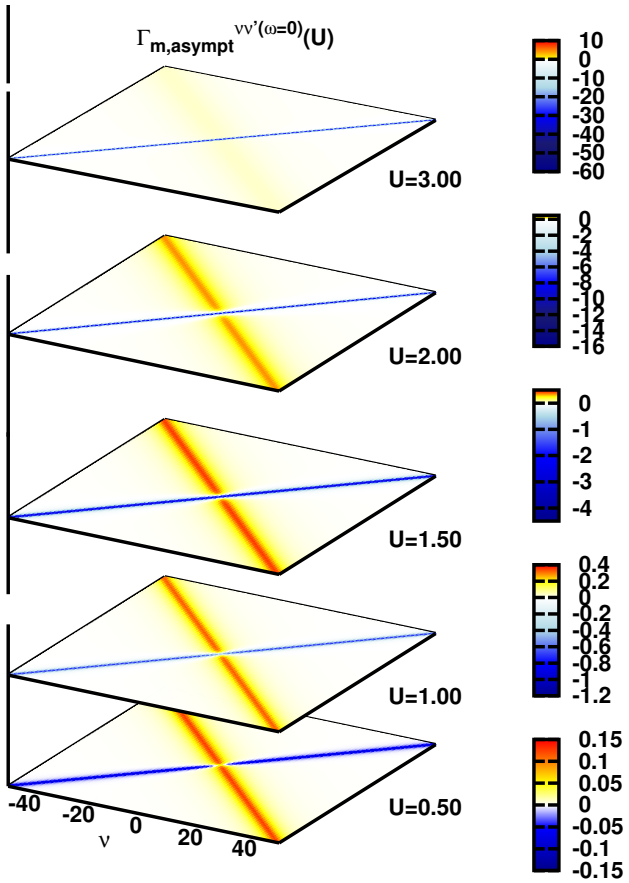

Figure 33: Layered density plot of $\Gamma^{\nu\nu'(\omega=0)}_{m,asympt}$ as function of $\nu, \nu^{'}$ for different values of U. Approaching the MIT leads to a strong enhancement of the main diagonal (blue colored), which corresponds to a strong enhancement of the χ_m contribution to $\Gamma_{m,asympt}$ in Eq. 122. χ_m contributes to $\Gamma_{m,asympt}$ with a minus sign (Eq. 123), which renders the corresponding main diagonal structure also negative (in contrast to Γ_d). Note the changes in the color scale for increasing U

4.2.3 Irreducible vertex functions in the asymptotic high-frequency regime

We will now investigate the asymptotic high frequency part of the irreducible vertex functions along different 1D-paths within the 3D-frequency space and compare it to the irreducible vertex functions, calculated via an inversion on a large frequency interval (320 fermionic frequencies). As we have seen in the previous chapter (Sec. 3), the irreducible vertex is a function of the two fermionic Matsubara frequencies ν and ν', and the bosonic matsubara frequency ω. For a better readability of the plots of the vertex function, we will present them as functions of the indices n,$n^{'}$ and m of the Matsubara frequencies, instead of the Matsubara frequencies themselves[5]

The frequency structure of Γ is presented in Fig. 34 for $\omega = 0$ and in Fig. 35 for $\omega = 20$ ($U = 1.00$ and $\beta = 26.0$) as a density plot in the $\nu\nu^{'}$-plane. In the asymptotic regime of the irreducible particle-hole vertex (Fig. 34, upper panels), the main structures of the vertex originate from diagrams, which are constant along $\nu - \nu^{'} = const$ and $\nu + \nu^{'} + \omega = const$ with a maximum at $\nu - \nu^{'} = 0$ and $\nu + \nu^{'} + \omega = 0$ (see Eq. 119, 122). As for the particle-particle sector, we have calculated the particle-particle vertex (Fig. 34, lower panel) employing the particle-particle frequency notation, one observes a similar structure as for the particle-hole vertex (a main diagonal and a secondary diagonal). However, the equation for the secondary diagonal within the particle-particle channel is now a function of $\omega - \nu - \nu^{'}$. An increasing ω leads to a shift of the secondary diagonal in the opposite direction compared to the particle-hole channel (Fig. 35). In Chap. 3 we have also analyzed the contribution of the fully irreducible parts to the asymptotics of the irreducible vertex functions, which we reduce to the constant U.[6] We can subtract this constant U contribution from the irreducible vertex without loosing any relevant information and concentrate on the frequency dependent contributions only. However for the plots along the most significant 1D-paths, we will keep the contribution of the fully irreducible parts to the asymptotics of the irreducible vertex functions in order to better quantify the relative error of the asymptotics and the relative error of the downfolded irreducible vertex functions in comparison to the numerical "exact" vertex functions.

[5]However, we will nevertheless keep the labels ν,$\nu^{'}$ and ω for the Matsubara frequency axes for the sake of a better readability

[6]$\Lambda_{\uparrow\downarrow,asympt} = +U$.
which leads to a constant background in the irreducible vertex functions Γ_{dmst}:
$\Gamma_{d,const} = +U$, $\Gamma_{m,const} = -U$, $\Gamma_{s,const} = +2U$, $\Gamma_{t,const} = 0$.

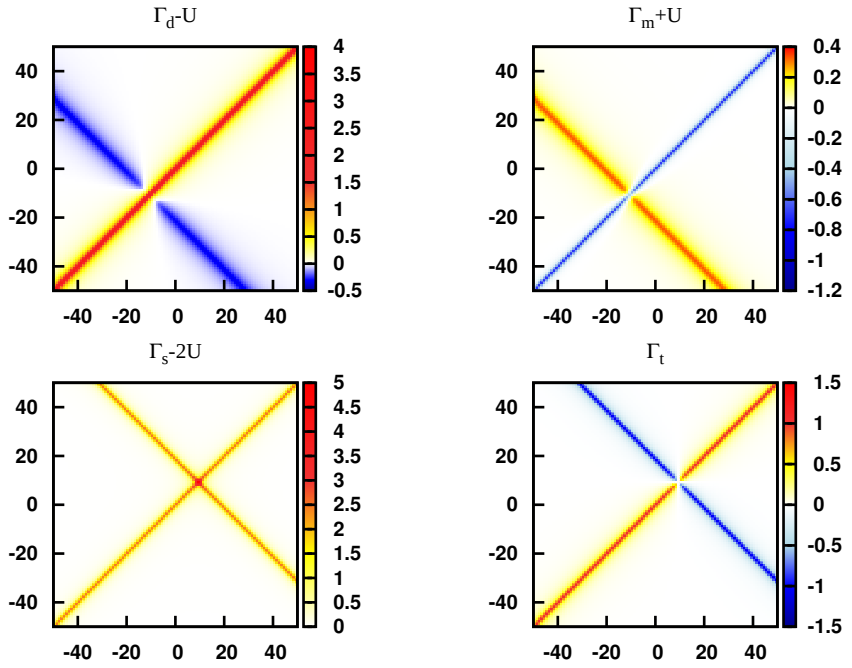

Figure 34: Densityplot of the irreducible vertex functions $\Gamma^{\nu\nu'(\omega=0)}_{dmst,asympt}$ for $\beta = 26.0$ and $U = 1.00$. The upper panel showing the density (left) and magnetic (right) channel. The particle-particle channel is shown in the lower panel (triplet channel lower-left and singlet channel lower-right). The background, caused by the bare interaction U has been subtracted

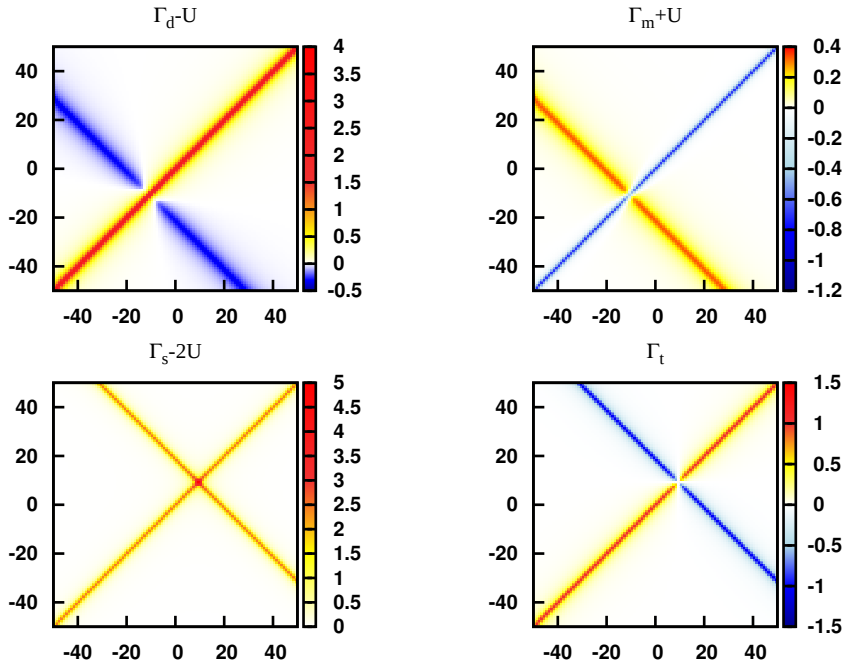

Figure 35: Densityplot of the irreducible vertex functions in the asymptotical high frequency regime $\Gamma_{dmst}^{\nu\nu'(\omega=20)}$ for $\beta = 26.0$ and $U = 1.00$. The upper panel showing the density (left) and magnetic (right) channel. The particle channel is shown in the lower panel (singlet channel lower-left and triplet channel lower-right). The background, caused by the bare interaction U has been subtracted

When using the vertex functions in its asymptotical form as input for the downfolding approach, one has to separate the regions (in the 3D frequency space), where the numerical inversion of the Bethe-Salpeter equations is strictly necessary from the regions, where one can use the asymptotic form of the irreducible vertex functions instead. In order to compare the numerical inversion of the Bethe-Salpeter equations on a large frequency range (320 fermionic frequencies) with the asymptotical form of the irreducible vertex functions, we have chosen the most significant 1D-paths in the (ν,$\nu^{'}$)-space for constant $\omega = 0, 20$, $U = 1.0, 1.5$ and $\beta = 26.0$. It is important to notice that for this comparison, we have chosen generic values for U and β, where we can show the similarities and discrepancies between the asymptotics and the numerical "exact" vertex functions in all four channels (density, magnetic, singlet, triplet) in the (ν,$\nu^{'}$)-space. However, comparison of the asymptotics with the numerical "exact" vertex functions has to be done over a larger U-range prior to implementation into existing computational procedures, which we will discuss in Chap. 5. In Fig. 36, we compare the asymptotical irreducible vertex functions with the irreducible vertex functions, calculated by inverting the Bethe-Salpeter equations on a 320 fermionic frequency range for $U = 1.0$ and $\omega = 0$ along the 1D-path $\nu = 0$[7]. Although truncating the inversion after 320 frequencies is still an ap-

[7]For better readability and to avoid any confusion, we keep the notation $\nu, \nu^{'}$ ω but show the numerical results as functions of $n, n^{'}$ and m (see footnote 5)

proximation to the "exact" inversion procedure, we use this numerical result as basis for the comparison with the asymptotics. As one can see in Fig. 36, the asymptotics almost coincides with the numerical "exact" value already outside a relatively small frequency range of about 40 frequencies ($|\nu^{'}| > 20$) in all four channels. In Fig. 37, we investigate the relative error of the asymptotics along the 1D-path $\nu = 0$ for $U = 1.00$. At $\nu^{'} = 20$, the largest relative error, appearing in Γ_m, is already below one percent. For the particle-hole channels, this result confirms similar observations by Jan Kuneš [33]. We note that for the triplet channel, the asymptotic approximation almost coincides with the exact value. In Figs. 34 and 35 the main frequency-structures of the irreducible vertex functions are along $\nu = \nu^{'}$, $\omega + \nu + \nu^{'} = const$ and $\omega - \nu - \nu^{'} = const$ for the particle-hole and particle-particle channels respectively. Therefore we also compare the asymptotic approximation with the exact results along $\nu = \nu^{'}$. In Fig. 38 we have plotted this path ($\nu = \nu^{'}$) for $U = 1.0$, $\omega = 0$ and $\beta = 26.0$. As one can observe, the asymptotics essentially coincides with the numerical "exact" value outside the same small frequency range of about 40 ($|\nu^{'}| > 20$) frequencies.

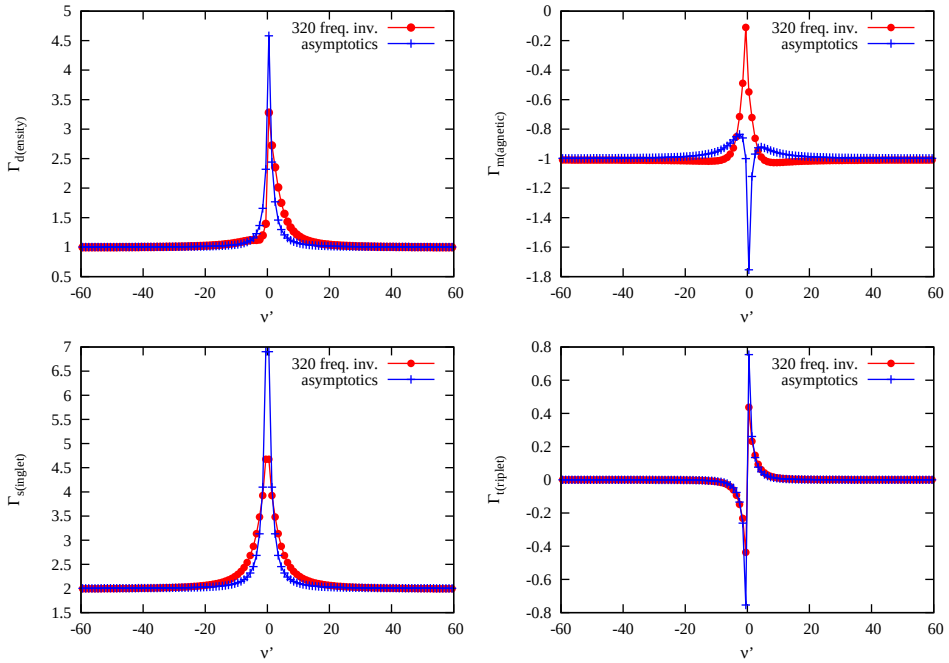

Figure 36: 1D plot of the irreducible asymptotic vertex functions compared to the irreducible vertex functions calculated for 320 fermionic frequencies, for $U = 1.00$, $\beta = 26.0$ and $\omega = 0$ at $\nu = 0$. The density and magnetic channel are in the upper left and upper right panel respectively. The singlet and triplet channel are in the lower left and right panel. The asymptotically calculated vertex functions are in very good agreement with the vertex functions calculated on a large fermionic frequency interval (320 frequencies) for $|\nu'| > 20$.

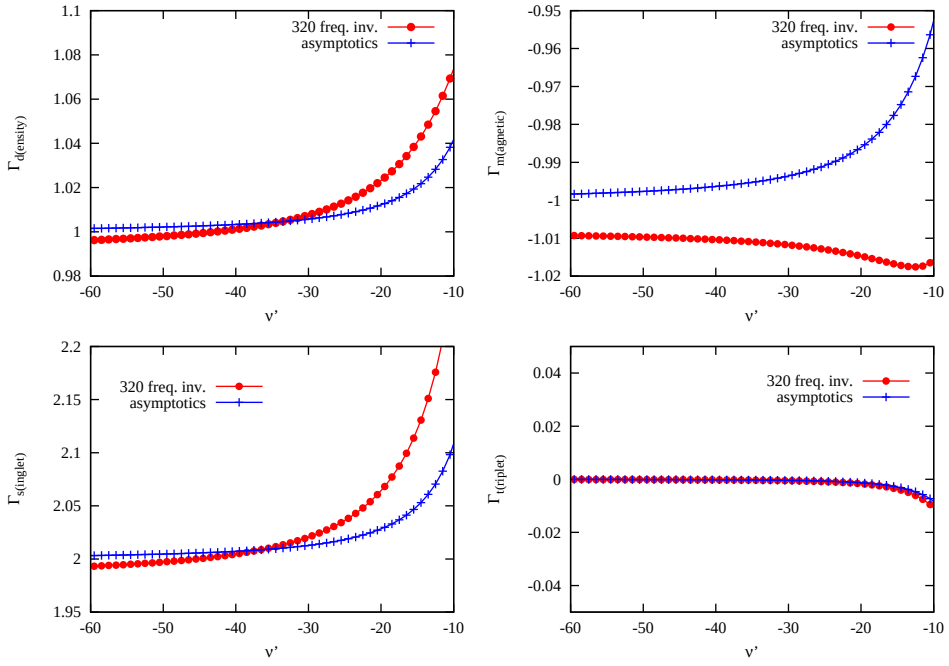

Figure 37: 1D plot of the irreducible asymptotic vertex functions compared to the irreducible vertex functions calculated for 320 fermionic frequencies. The plot is showing a 1D-path of Γ_{dmst} along $\nu = 0$ for $U = 1.00$, $\beta = 26.0$, $\omega = 0$ within a small frequency range (between $\nu^{'} = -10$ and $\nu^{'} = -60$) . At $\nu^{'} = 20$, the largest relative error, appearing in Γ_m is already below one percent

If we compare the vertex functions with its asymptotical form along the 1D-path $(\nu = 0, \nu^{'})$ as for $U = 1.0$ (Fig. 36) also for $U = 1.5$ (Fig. 39), we identify the same frequency range ($|\nu^{'}| > 20$), where the asymptotical high frequency irreducible vertex functions coincide with the numerical "exact" vertex functions. Therefore, one can assume a U-independent frequency range, where one can safely replace the numerical "exact" vertex by its asymptotical form. Let us mention another interesting observation when comparing Γ_d for $U = 1.0$ and $U = 1.5$:

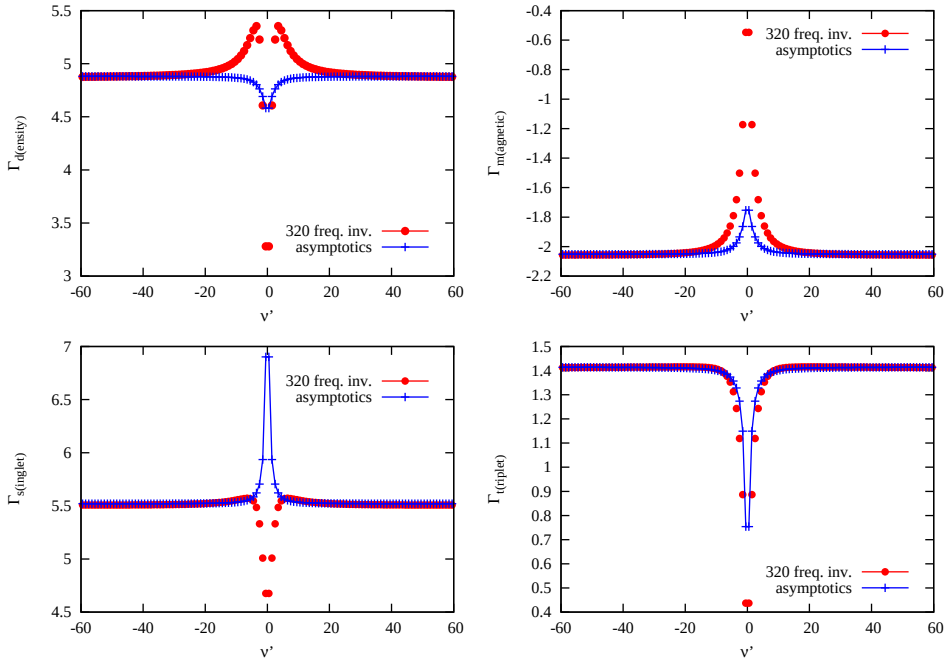

Figure 38: 1D plot of the irreducible asymptotic vertex functions compared to the irreducible vertex functions calculated for 320 fermionic frequencies, for $U = 1.00$, $\beta = 26.0$ and $\omega = 0$ at $\nu = \nu^{'}$.

The graphs of the exact vertex functions are completely different in the low-frequency regime. This behavior is consistent with recently discovered low-frequency divergencies in Γ_d for U-values definitely smaller than U_{crit} (U at the Mott transition point) [55]. Interestingly, the high-frequency behavior is not affected by this singularity, as one can clearly see by comparing the asymptotic vertex functions for $U = 1.0$ and $U = 1.5$ in Figs. 36 and 39. Let us stress that, though these low frequency divergencies con be considered as precursors of the MIT, they are completely different from the high frequency divergencies along $\nu = \nu^{'}$ of Γ_{dmst}, discussed in Sec. 4.2.2.

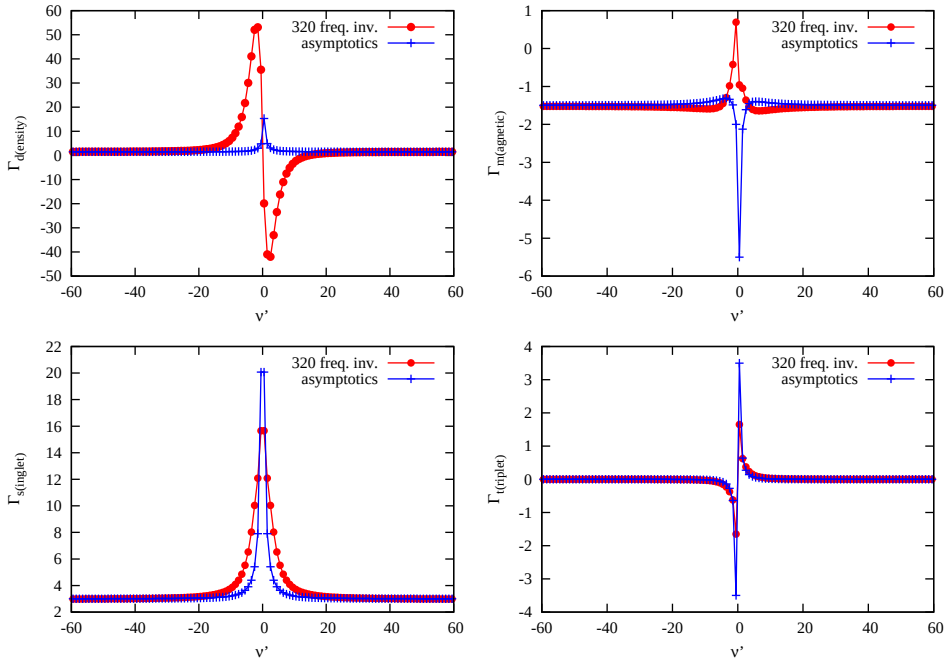

Figure 39: 1D plot of the irreducible asymptotic vertex functions compared to the irreducible vertex functions calculated for 320 fermionic frequencies, for $U = 1.50$, $\beta = 26.0$ and $\omega = 0$ at $\nu = 0$. The density and magnetic channel are in the upper left and upper right panel respectively. The singlet and triplet channel are in the lower left and right panel. One can see an enhancement of the asymptotical high frequency irreducible vertices (blue) compared to $U = 1.00$ (Fig. 36). For the numerical "exact" vertices, $\Gamma_{density}$ obeys a rather different behavior at lower frequencies compared to $U = 1.00$

Hitherto, we have only discussed the irreducible vertex functions in their asymptotical form for $\omega = 0$ similarly as what was already done for the particle-hole channel in Ref. [33]. From now on, we will also compare the asymptotics with the numerical "exact" value for finite ω. In Fig. 40, we have plotted the irreducible vertex functions Γ_{dmst} for $(U = 1.0, \beta = 26.0, \omega = 20, \nu = 0, \nu^{'})$. Two main structures, at $\nu^{'} = 0$ and $\nu^{'} = 20$ for the singlet/triplet channel, and $\nu^{'} = -20$ for the density/magnetic channel are obtained. The reason behind this is that the asymptotic vertex functions $\Gamma_{dm,asympt}$ and $\Gamma_{st,asympt}$ depend only on $(\nu - \nu^{'})$ and $(\nu + \nu^{'} + \omega)$ (for $\Gamma_{dm,asympt}$) and $(-\nu - \nu^{'} + \omega)$ (for $\Gamma_{st,asympt}$) via the susceptibilities $\chi_{d,m}(\nu - \nu^{'})$, $\chi_{d,m}(\omega - \nu - \nu^{'})$ and $\chi_{pp}(\nu + \nu^{'} + \omega)$. As one can see for $(\nu = 0, \nu^{'})$ in Fig. 40 and also $(\nu = \nu^{'})$ in Fig. 41, this affects also the frequency range, where we safely can use the asymptotics instead of the numerical "exact" vertex. This is now "shifted" by $\pm\frac{\omega}{2}$ for the density/magnetic and singlet/triplet channel respectively. We observe moreover, that the frequency range, where we still have to invert the Bethe-Salpeter equations numerically, has also to be enlarged w.r.t the case $\omega = 0$. For $\omega = 20$ (e.g. Fig. 41) a frequency range of $(-40 < \nu < 20)$ for the density/magnetic and $(-20 < \nu < 40)$ for the singlet/triplet channel should be sufficient according to Figs. 40 and 41.

This happens because the frequency region, where one has to actually invert the Bethe-Salpeter equations does now contain two main structures: at $\nu^{'} = 0$ and $\nu^{'} = \pm\omega$ for the density/magnetic and singlet/triplet channel respectively. Summing up the observations from Figs. 40 and 41, the frequency-interval where the numerical inversion is mandatory should be defined as:

Inversion-range: $[-Max - \omega, Max]$ (for the density/magnetic channel)
Inversion-range: $[-Max, Max + \omega]$ (for the particle-particle channel),

where Max is the lowest frequency $|\nu|$, where one can replace the "exact" vertex by its asymptotical form, at $\omega = 0$ (in our previous cases $Max = 20$).

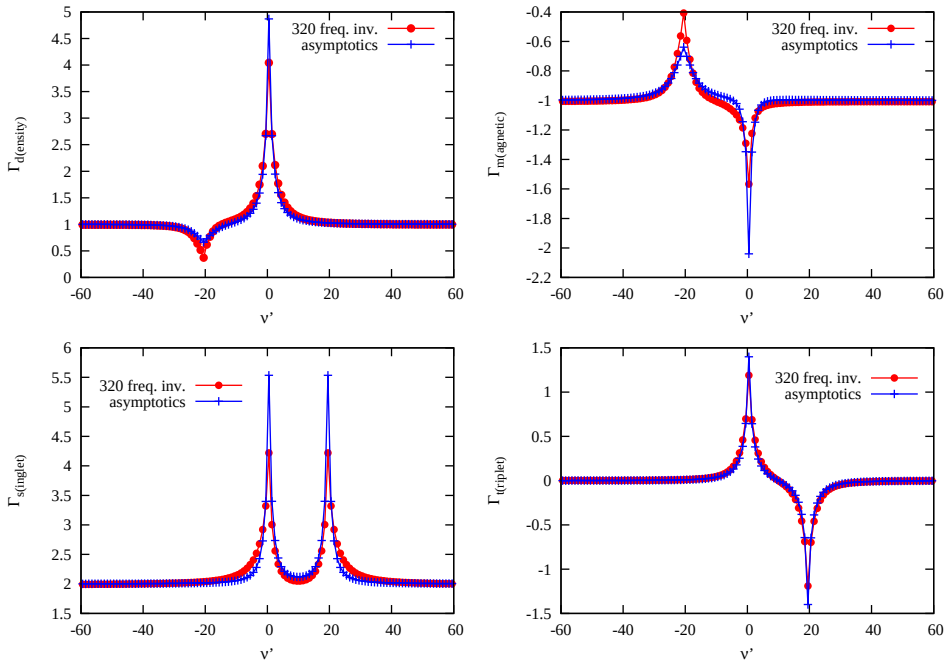

Figure 40: 1D plot of the irreducible asymptotic vertex functions compared to the irreducible vertex functions calculated for 320 fermionic frequencies, for $U = 1.00$, $\beta = 26.0$ and $\omega = 20$ at $\nu = 0$.

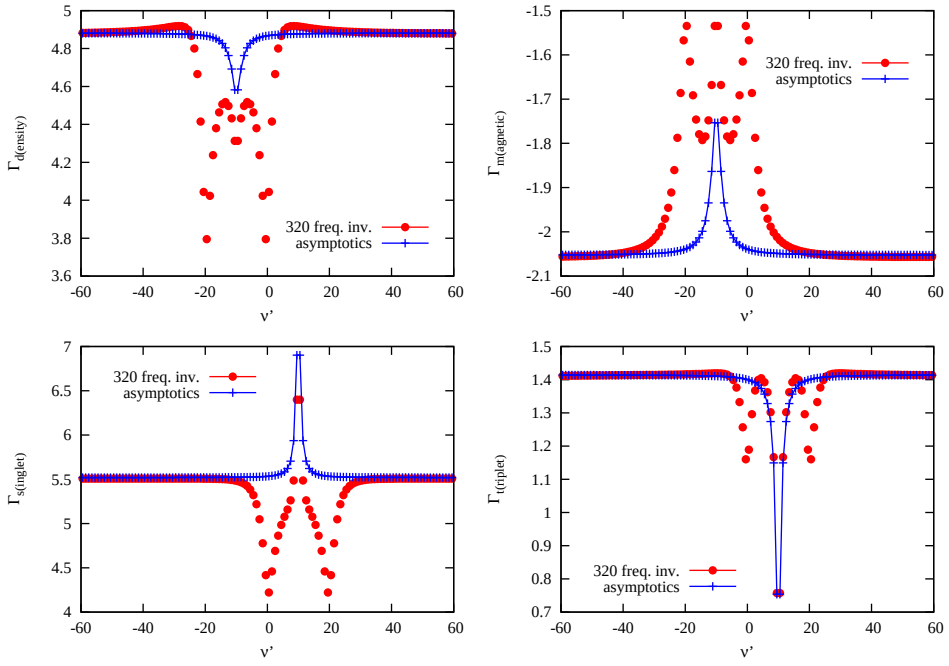

Figure 41: 1D plot of the irreducible asymptotic vertex functions compared to the irreducible vertex functions calculated for 320 fermionic frequencies, for $U = 1.00$, $\beta = 26.0$ and $\omega = 20$ at $\nu = \nu^{'}$.

4.3 Application of the Downfolding procedure

4.3.1 Downfolding for $\omega = 0$

In Sec. 3.4 we have illustrated a method for the calculation of the low frequency part of the irreducible vertex functions Γ by inverting a truncated Bethe-Salpeter equation and adding a correction term, which includes the high-frequency asymptotics of the Γ's. These treatments extends the work of Jan Kuneš [33] to all channels and bosonic frequencies $\omega \neq 0$. Since the computational effort for calculating the asymptotics of the Γ's is much lower than for the inversion of the Bethe-Salpeter equation (or more precisely for the calculation of the generalized susceptibilities $\chi^{\nu\nu^{'}\omega}_{dmst}$), we were able to calculate the asymptotics on a significantly larger frequency range (we have calculated the asymptotics on a 1600 frequency range. However, in principle one could also perform the calculation on a much larger frequency range). In the following, we show the applicability of the downfolding by computing the vertex functions in all four channels (d,m,s,t) using the new downfolding algorithm developed in Sec. 3.4 and compare it with the vertex functions calculated from an inversion in a large frequency range (320 frequencies), which we assume to be the exact result. We first discuss the results for the $\omega = 0$ case and will later extend our considerations to the $\omega \neq 0$ case. To compare the results for different inversion ranges, we show 1D plots along different paths within the 2D $(\nu, \nu^{'}; \omega = const)$ frequency space. According to our previous considerations about the asymp-

totics, we choose now the most significant paths, $\nu = 0, \nu = \nu^{'}$ and $\nu = -\nu^{'}$. In Fig. 42, we compare the vertex functions for $U = 1.0$ and $\beta = 26.0$ calculated on a large frequency range (320 freq. red line), with the vertex functions calculated with 40 frequencies for the inversion (green line). While for Γ_t, the small frequency range for inversion has no significant effect on the vertex function[8], the vertex functions in the other channels, calculated on a small frequency range, are different from the numerical "exact" ones throughout the considered frequency interval (green line). If we now add the correction terms derived in Sec. 3.4 (Eq. 108, Eq. 111 and Eq. 114) to the vertex functions which have been calculated on the smaller frequency interval (40 frequencies), we obtain a significant improvement, with results approaching the numerical "exact" functions. However, a closer inspection of, e.g., $\Gamma_{density}$ (e.g. for $\nu = \nu^{'}$ in Fig. 43 or $\nu = -\nu^{'}$ in Fig. 44), indicates an overcorrection since the corrected vertex function now lies slightly above the numerical "exact" value. We will discuss this issue when we describe the limitations and conclusions of the downfolding procedure at the end of this chapter.

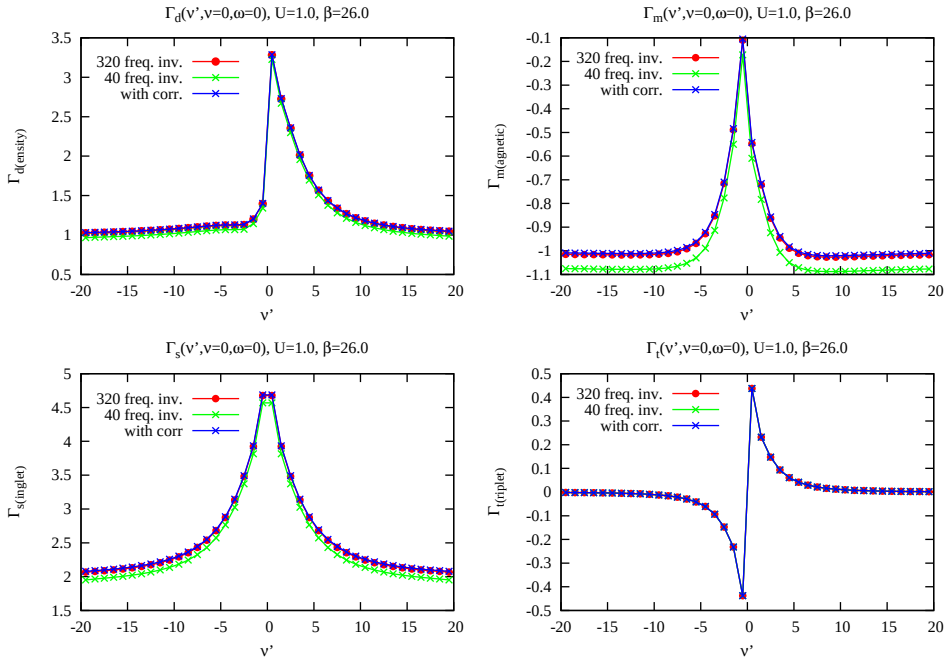

Figure 42: Comparison of the irreducible vertex functions calculated on a large frequency interval (320 frequencies, red line), to the corresponding vertex function calculated in a small frequency range (40 frequencies, green line) + correction term from the downfolding (blue line). The plot is showing a 1D-path of Γ_{dmst} along $\nu = 0$ for $U = 1.00$, $\beta = 26.0$, $\omega = 0$

[8]This is analog to the atomic limit result in [44] where $\Gamma_t^{\nu\nu^{'}(\omega=0)}$ was shown to be $\propto (\delta_{\nu\nu'} + \delta_{\nu(-\nu'}$

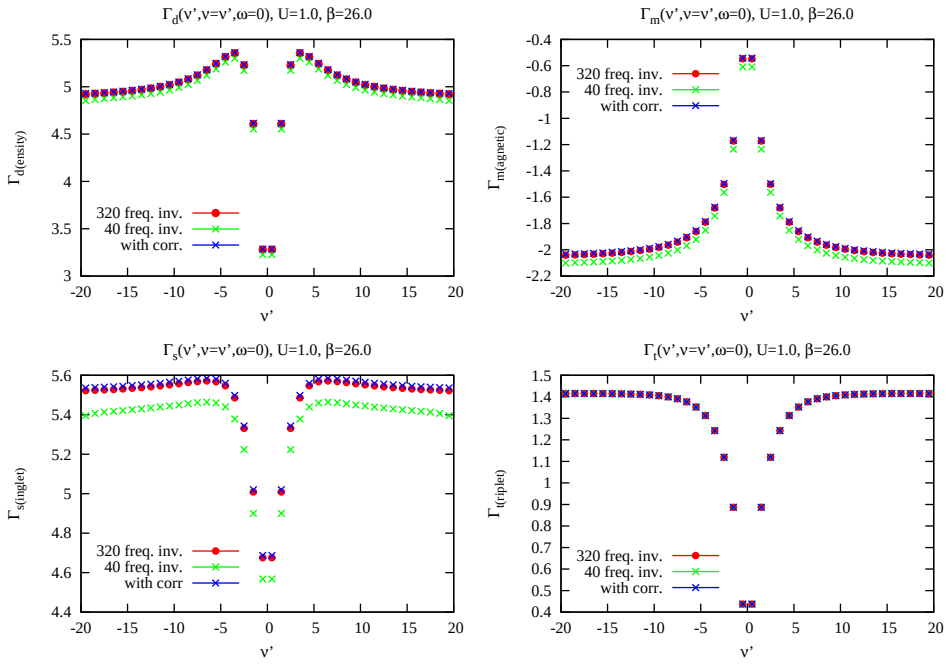

Figure 43: Comparison of the irreducible vertex functions calculated on a large frequency interval (320 frequencies, red line), to the corresponding vertex function calculated on a small frequency range (40 frequencies, green line) + correction term from the downfolding(blue line). The plot is showing a 1D-path of Γ_{dmst} along $\nu = \nu^{'}$ for $U = 1.00$, $\beta = 26.0$, $\omega = 0$. One observes a slight overcorrection of the vertex functions calculated on a drastically truncated frequency range (blue line) compared to the vertex functions calculated on a large frequency interval

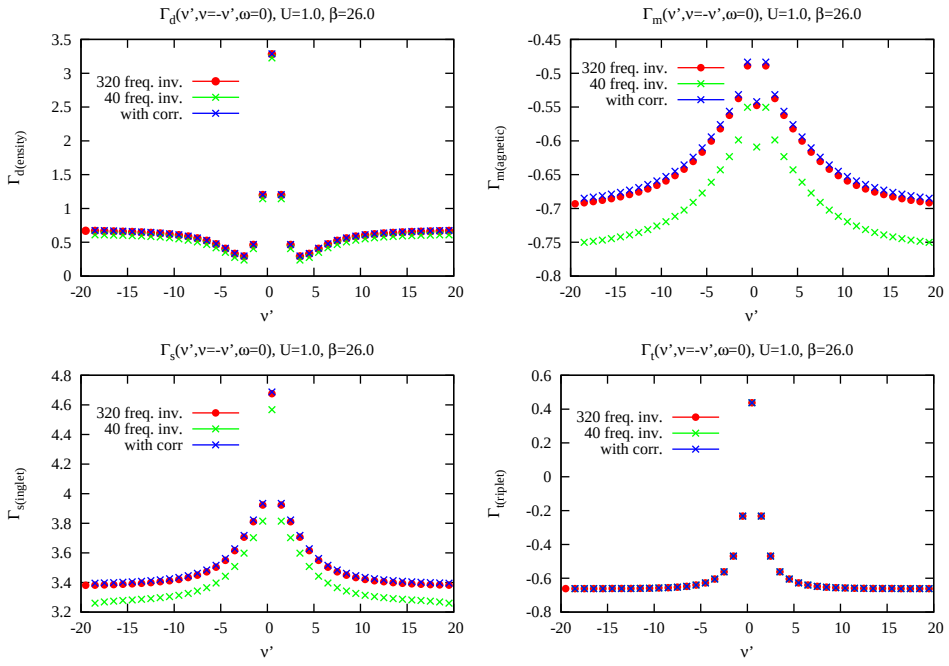

Figure 44: Comparison of the irreducible vertex functions calculated on a large frequency interval (320 frequencies, red line), to the corresponding vertex function calculated on a small frequency range (40 frequencies, green line) + correction term from the downfolding (blue line). The plot is showing a 1D-path of Γ_{dmst} along $\nu = -\nu^{'}$ for $U = 1.00$, $\beta = 26.0$, $\omega = 0$. One observes a slight overcorrection of the vertex functions calculated on a drastically truncated frequency range (blue line) compared to the vertex functions calculated on a large frequency interval

Consistently with the analysis of the previous section, if we increase U (e.g. to $U = 1.50$ in Fig. 45), the relative error of the vertex functions calculated on the small frequency interval compared to the vertex functions calculated on the large frequency interval has basically not changed compared to a smaller U. At the same time, the size of the frequency interval of the actual inversion of the Bethe-Salpeter equations obviously strongly affects the quality of the results: In Fig. 46 and Fig. 47, we have calculated the irreducible vertex functions on a larger frequency range (80 frequencies). In comparison to the smaller frequency interval of 40 frequencies (Fig. 42 and Fig. 43) one observes a significant enhancement of the non-corrected vertex functions (green line). However, the important finding here is that in both cases, adding the corresponding correction terms (blue line) lead essentially to the same result. This demonstrates the validity of the downfolding procedure.

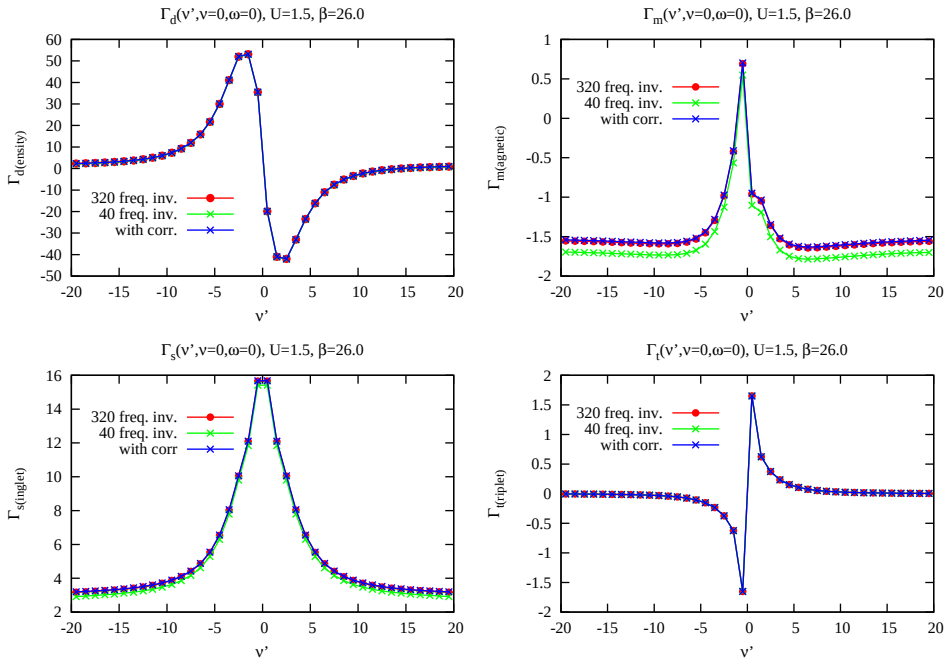

Figure 45: Comparison of the irreducible vertex functions calculated on a large frequency interval (320 frequencies, red line), to the corresponding vertex function calculated on a small frequency range (40 frequencies, green line) + correction term from the downfolding (blue line). The plot is showing a 1D-path of Γ_{dmst} along $\nu = 0$ for $U = 1.50$, $\beta = 26.0$, $\omega = 0$. In comparison to a smaller U (e.g. $U = 1.00$ in Fig. 42), the relative error has not changed

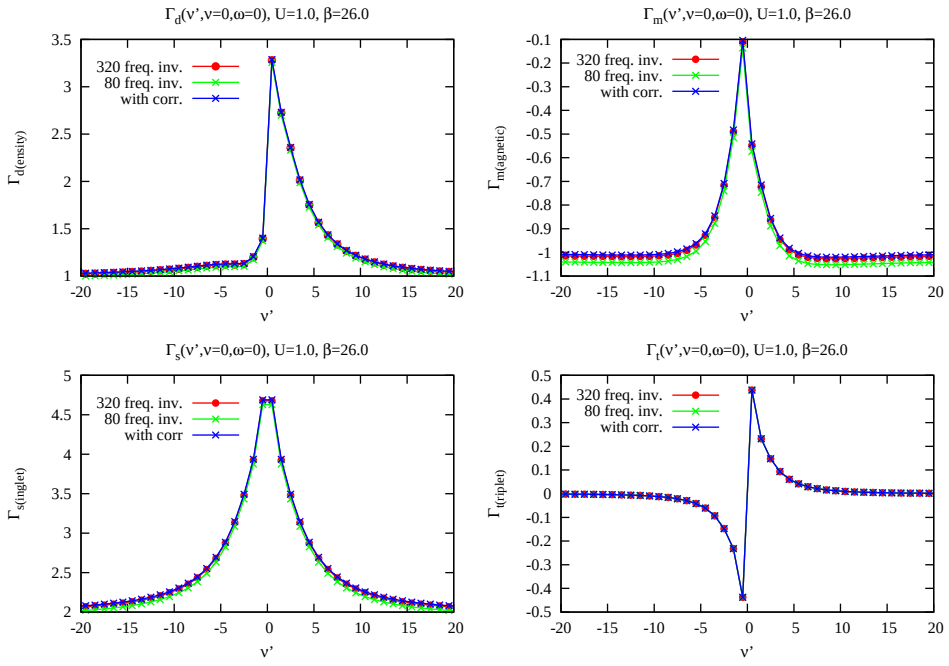

Figure 46: Comparison of the irreducible vertex functions calculated on a large frequency interval (320 frequencies, red line), to the corresponding vertex function calculated on a small frequency range (80 frequencies, green line) + correction term from the downfolding (blue line). The plot is showing a 1D-path of Γ_{dmst} along $\nu = 0$ for $U = 1.00$, $\beta = 26.0$, $\omega = 0$. The uncorrected vertex functions (green line) are now closer to the numerical "exact" ones (red line), compared to the smaller frequency interval (40 frequencies) in Fig. 42. However, adding the correction term lead to the same result for both frequency intervals (blue line), showing the strength of the downfolding procedure

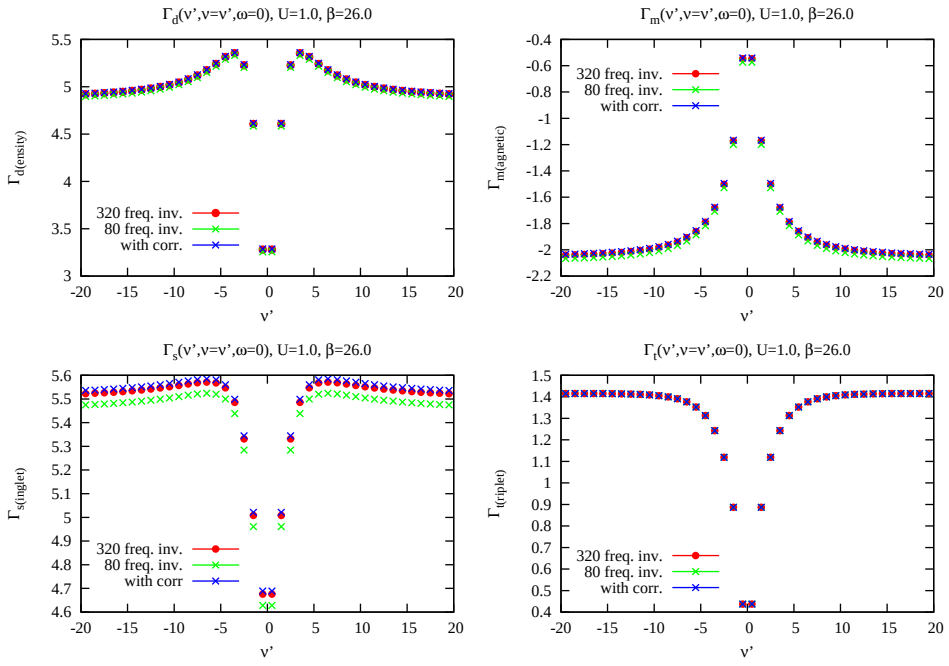

Figure 47: Comparison of the irreducible vertex functions calculated on a large frequency interval (320 frequencies, red line), to the corresponding vertex function calculated on a small frequency range (80 frequencies, green line) + correction term from the downfolding (blue line). The plot is showing a 1D-path of Γ_{dmst} along $\nu = \nu^{'}$ for $U = 1.00$, $\beta = 26.0$, $\omega = 0$. The uncorrected vertex functions (green line) are now closer to the numerical "exact" ones (red line), compared to the smaller frequency interval (40 frequencies) in Fig. 43. However, adding the correction term lead to the same result for both frequency intervals (blue line), showing the validity of the downfolding procedure

In summary, we have shown numerically how the correction terms calculated by the downfolding procedure for $\omega = 0$ significantly improve the results of the calculation of the irreducible vertex functions on a small frequency interval. We didn't observe any major influence of different U's on the quality of the correction terms. Furthermore, also larger errors, obtained by the usage of smaller frequency intervals, were successfully corrected. In Figs. 48 and 49 we have compared the irreducible vertex functions calculated on a 40- and 80-frequency interval respectively (green line), with the irreducible vertex functions calculated on a large frequency interval (320 frequencies, red line) for $U = 1.00$ again, but now zoomed into a tiny range within $\nu^{'} = -15$ and $\nu^{'} = -5$. The relative error of the irreducible vertex function calculated on a 40-frequency interval compared to the "exact-result" in the selected area (between $\nu^{'} = -15$ and $\nu^{'} = -5$) is about 6 % (e.g. for Γ_d). For the 80-frequency interval, the relative error dropped down to approximately 2 % (for Γ_d). However for both frequency intervals (40- and 80-frequencies), adding the corresponding correction term lead to a relative error of approx. 0.4 %. As we will see in the next section, the minimal frequency interval, we have to use for the exact

inversion of the Bethe-Salpeter equations depends on the bosonic Matsubara frequency ω.

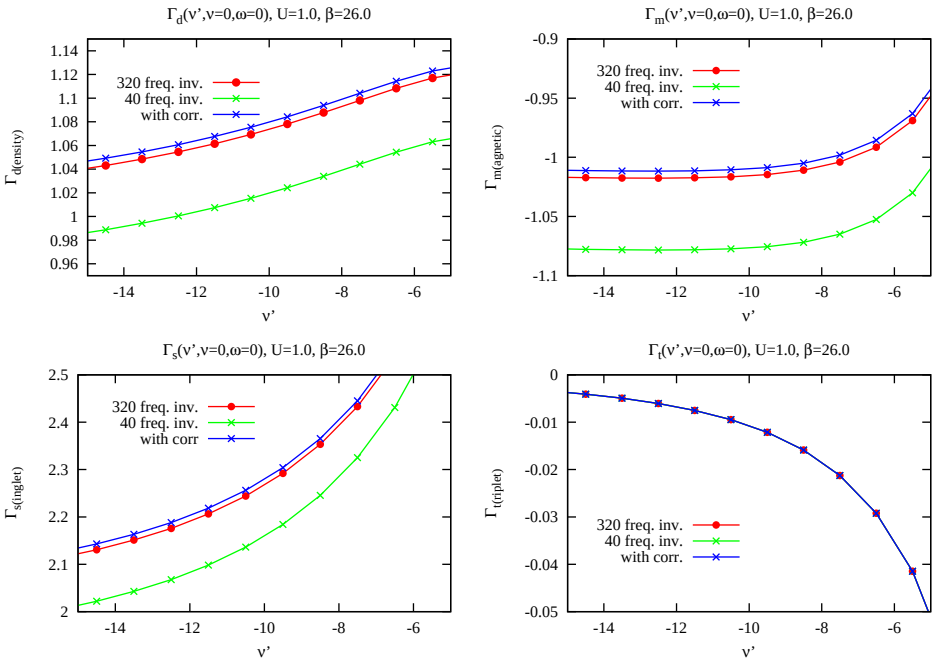

Figure 48: Comparison of the irreducible vertex functions calculated on a large frequency interval (320 frequencies, red line), to the corresponding vertex function calculated on a small frequency range (40 frequencies, green line) + correction term from the downfolding (blue line). The plot is showing a 1D-path of Γ_{dmst} along $\nu = 0$ for $U = 1.00$, $\beta = 26.0$, $\omega = 0$ within a small frequency range (between $\nu^{'} = -15$ and $\nu^{'} = -5$) . For Γ_d, the relative error of the uncorrected irreducible vertex function calculated on the small frequency range is approx. 6 percent. The relative error of the corrected irreducible vertex function is about 0.4 percent

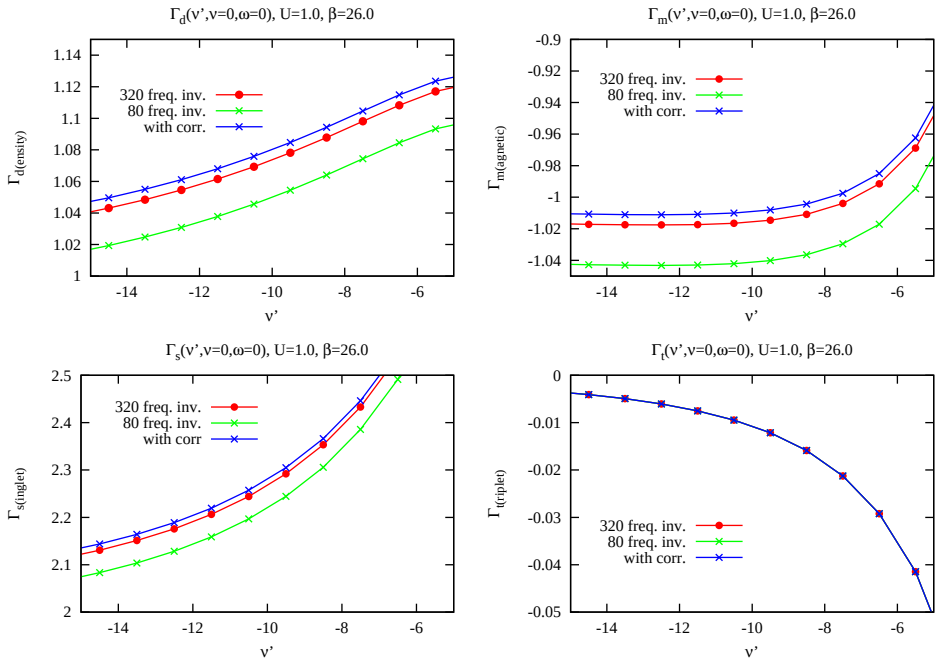

Figure 49: Comparison of the irreducible vertex functions calculated on a large frequency interval (320 frequencies, red line), to the corresponding vertex function calculated on a small frequency range (80 frequencies, green line) + correction term from the downfolding (blue line). The plot is showing a 1D-path of Γ_{dmst} along $\nu = 0$ for $U = 1.00$, $\beta = 26.0$, $\omega = 0$ within a small frequency range (between $\nu^{'} = -15$ and $\nu^{'} = -5$) . For Γ_d, the relative error of the uncorrected irreducible vertex function calculated on the small frequency range is approx. 2 percent. The relative error of the corrected irreducible vertex function is about 0.4 percent

4.3.2 Downfolding for $\omega \neq 0$

If we turn to the $\omega \neq 0$ case, we again have to define regions where numerical inversion is mandatory and, in contrast, where we can approximate using our asymptotic results, respectively. We can identify the regions of interest by considering the involved diagrams of the respective irreducible channels. For the particle-hole channels, e.g., the second order bubble diagram (longitudinal) is proportional to

$$P_1 = G(\nu)G(\nu + \omega) \tag{124}$$

Since the Green functions are proportional to $\frac{1}{\nu}$ and $\frac{1}{\nu+\omega}$ respectively, the main contribution of P_1 to the irreducible particle-hole channel will be around $\nu = 0$ and $\nu = -\omega$ (For the particle-particle channel it can be shown, that the main contributions are around $\nu = 0$ and $\nu = +\omega$). Therefore for the $\omega = 0$ case, we were able to center our inversion interval around $\nu = 0$, i.e. [-Max,+Max]. At finite ω, our inversion interval will change, according to

$$[-Max... + Max] \stackrel{ph}{\rightarrow} [-Max - \omega... + Max] \tag{125}$$

and

$$[-Max... + Max] \stackrel{pp}{\rightarrow} [-Max... + Max + \omega]. \tag{126}$$

From an algorithmic point of view, it is better to center our inversion interval around $\frac{\omega}{2}$ and $-\frac{\omega}{2}$ for the particle-particle and particle-hole channel respectively. This is evidently consistent with observations about the vertex asymptotics of the previous section. In order to check the quality of the downfolding procedure for finite ω, we choose significant paths for our plots, $\nu = \nu^{'}$, $\nu = 0$ and $\nu = \pm\omega$. The main difference due to a finite ω can be observed, e.g. in the $\Gamma_{singlet}$ channel, where the two main structures are clearly separated (see e.g. Fig. 50 for a 40 frequency inversion interval). If one reduces the interval below a critical value (evidently dependent on the ω we use), the main structures in the small interval would be cut off. Since, in this procedure, the whole irreducible vertex is computed as the inversion interval + its asymptotics, we would replace parts of the main structure with the asymptotic value of the vertex function, which is obviously wrong. Hence, for increasing ω, the inversion interval, and therefore the computational effort gets progressively larger. This is obviously a limiting factor of the whole downfolding procedure. However, there is still potential for algorithmic improvements in this respect which we will discuss at the end of the chapter.

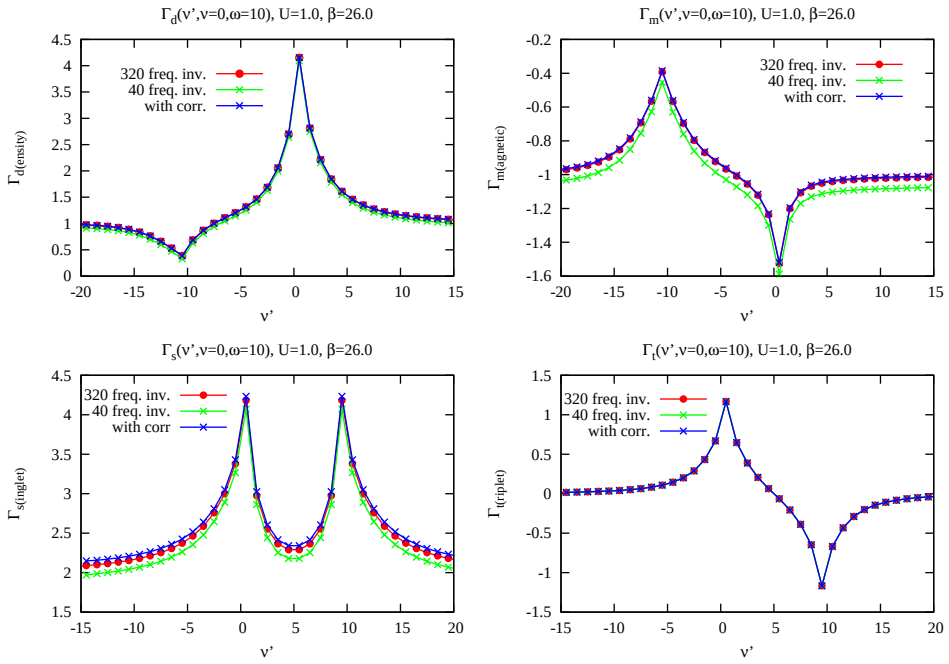

Figure 50: 1D-plot of the Vertex functions for $\nu = 0$, $U = 1.0$, $\beta = 26.0$ and $\omega = 10$ with exact inversion of 320 frequencies compared to the 40 frequency inversion (with and without the correction calculated with the downfolding formula). The inversion interval is centered around $-\frac{\omega}{2}$ for the ph-channels and $+\frac{\omega}{2}$ for the particle-particle channels. In the Γ_s plot at the left bottom, one clearly identifies the two main structures around $\nu = 0$ and $\nu = \omega$

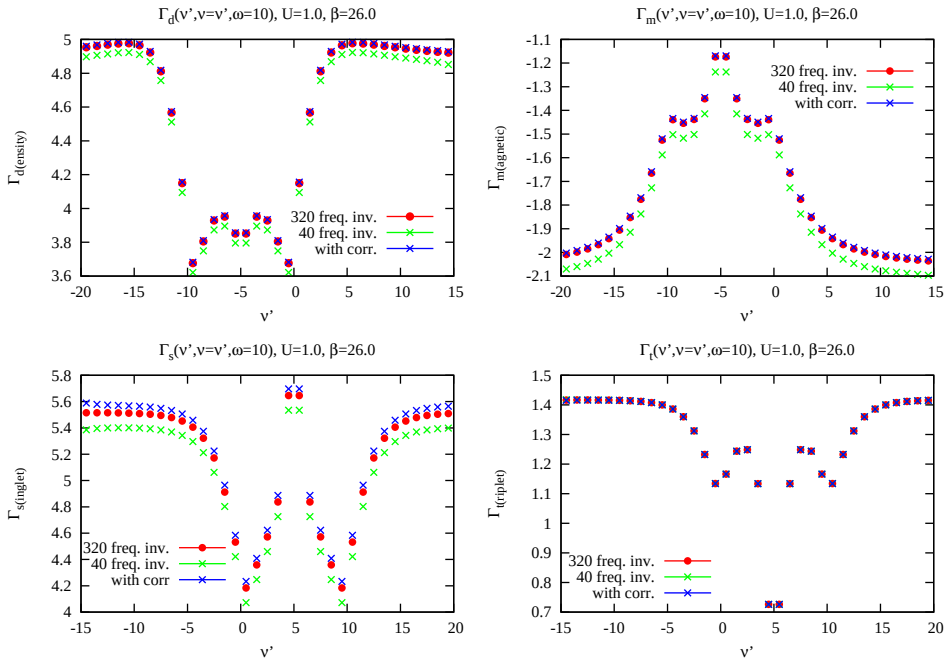

Figure 51: 1D-plot of the Vertex functions for $\nu = \nu^{'}$, $U = 1.0$, $\beta = 26.0$ and $\omega = 10$ with exact inversion of 320 frequencies compared to the 40 frequency inversion (with and without the correction calculated with the downfolding formula). The inversion interval is centered around $-\frac{\omega}{2}$ for the ph-channels and $+\frac{\omega}{2}$ for the particle-particle channels. In the Γ_s plot at the left bottom, one clearly identifies the two main structures around $\nu = 0$ and $\nu = \pm\frac{\omega}{2}$

4.4 Evaluation and Limits of the Downfolding procedure

In the previous section, we illustrated the power of the developed downfolding procedure based on the comparison of a strongly reduced inversion interval (40,80 frequencies) to a large one (320 frequencies). We observed a remarkable improvement of the results, when adding a correction term, calculated on basis of the asymptotic behavior of the vertex functions, which have been calculated on a significantly larger frequency interval (1600 frequencies). However, a closer look on the results (e.g. Fig. 42) reveals a slight overcorrection (red dots are slightly below the blue ones). Up to now, there is no clear explanation for this behavior, nevertheless, a hand waving argument based on the results can be given. The downfolding procedure for the larger inversion intervals (80 and higher) frequencies is very stable and leads to the same overcorrection. Therefore, the irreducible vertex function obtained by the downfolding procedure is more likely to be close to the exact function.

Another problem within the downfolding procedure is the growing inversion interval for finite ω. As was mentioned in the discussion, we centered the interval around $\pm\frac{\omega}{2}$ and extended it to $[-Max-\omega...Max]$ and $[-Max...Max+\omega]$ for the particle-hole and particle-particle channel respectively. The parameter Max

is the critical parameter regarding the accuracy of the calculation. For large ω, the performance of the procedure gets worse since a large inversion interval is needed to include the structures at $\nu = 0$ and $\nu = \pm\omega$. If we consider, e.g. the Γ_s of Fig. 50, we observe a clear separation of the two structures proportional to ω. However the good news is that, if ω gets larger, we can again approximate the region in between $\nu = 0$ and $\nu = \pm\omega$ by its asymptotic form. Therefore, a possible improvement could be a recursive procedure, where one alternately replaces the first structure with the asymptotics and calculates the second one.

5 Summary and Outlook

In my thesis, I have derived the expressions for the two-particle irreducible vertex functions of DMFT in all channels and for all bosonic (transfer) frequencies in the high-frequency asymptotic regime. After showing, how the hallmarks of the Mott-Hubbard MIT are also visible in the vertex asymptotics, I moved to consider some important algorithmic aspects. In particular, I have compared the asymptotical irreducible vertex function with the exact vertex function calculated via an inversion on a large frequency interval (320 fermionic frequencies). For $\omega = 0$ the asymptotics coincides with the numerical "exact" value outside a small frequency range of about 40 frequencies in all channels (spin, charge, singlet, triplet). Hence one can replace the numerical "exact" vertex by its asymptotic form over a large frequency range. This is a major improvement over existing methods for calculating irreducible vertex functions, since the computational effort for calculating the asymptotic form of the irreducible vertex is significantly lower than the numerical inversion on a large frequency range. Specifically, I have shown that the size of the frequency range, where one still needs to invert the Bethe-Salpeter equations seems not to be affected by the value of U considered, but gets larger with increasing ω, thus increasing the computational effort. However, as I have proposed in Sec. 4.4, one can still approximate the region between $\nu = 0$ and $\nu = \pm\omega$ by its asymptotic form for larger ω, hence reducing the computational effort again. These considerations have an important impact on future algorithmic developments. In fact, if one aims at reducing the numerical effort, the full vertex calculations as well as the inversion of the inversion of the Bethe-Salpeter equations have to be done in the smallest possible frequency interval. In this respect, as I have shown in Chap. 4, the systematic error we make by truncation of the frequency range for the inversion can successfully be compensated by adding a correction term. Following the derivation by Jan Kuneš [33], I was able to calculate the correction term by means of a downfolding algorithm, which I have extended to the particle-particle channels and to finite ω. For further improvement and implementation of the presented asymptotic approximation and the downfolding procedure, additional tests have to be done, which are beyond the scope of this thesis. In particular, although I have shown the U-independence of the frequency regime where one can replace the numerical "exact" vertex by its asymptotic form, I have only presented data available for U values below the MIT ($U < U_{crit}$). Therefore comparison of the asymptotic high-frequency irreducible vertex function with the numerical "exact" vertex above U_{crit} should be done prior to implementation. Furthermore, I have proposed an extension to the developed downfolding method in Sec. 4.4, which clearly indicates the direction to continue the work of my Diploma thesis. In fact, the implementation of the proposed recursive procedure could significantly enhance the performance of the calculation of the irreducible vertex functions $\Gamma^{\nu\nu'\omega}_{dmst}$ for all ν,ν' and ω. Such developments can be potentially of a very high impact for the algorithmic improvements of all diagrammatic extensions of DMFT, which requires accurate calculations of local two-particle vertex functions as a starting point.

References

[1] P. Hohenberg W. Kohn, *Inhomogeneous Electron Gas*, Physical Review, **136** (1964).

[2] W. Kohn L. Sham, *Self-Consistent Equations Including Exchange and Correlation Effects*, Physical Review, **140** (1965).

[3] P. Blaha, K. Schwarz, P. Sorantin, *Full-potential, linearized augmented plane wave programs for crystalline systems*, Computer Physics Communications, **59**, 399 (1990).

[4] K. Schwarz P. Blaha, *Solid state calculations using WIEN2k*, Computational Materials Science, **28**, 259 (2003).

[5] *http://www.wien2k.at.*

[6] G. Kresse J. Hafner, *Ab initio molecular dynamics for liquid metals*, Physical Review B, **47** (1993).

[7] G. Kresse J. Furthmueller, *Efficiency of ab-initio total energy calculations for metals and semiconductors using a plane-wave basis set*, Computational Materials Science, **6**, 15 (1996).

[8] J. Hafner, *Ab-initio simulations of materials using VASP: Density-functional theory and beyond*, Journal of Computational Chemistry, **29**, 2044 (2008).

[9] *http://www.vasp.at.*

[10] D. McWhan, T. Rice, J. Remeika, *Mott Transition in Cr-Doped V_2O_3*, Physical Review Letters, **23** (1969).

[11] R. Kusters, J. Singleton, D. Keen, R. McGreevy, W. Hayes, *Magnetoresistance measurements on the magnetic semiconductor $Nd_{0.5}Pb_{0.5}MnO_3$*, Physica B, **155**, 362 (1989).

[12] J. Bednorz K. Müller, *Possible High Tc Superconductivity in the Ba-La-Cu-O System*, Zeitschrift für Physik B, **64**, 189 (1986).

[13] Y. Kamihara, T. Watanabe, M. Hirano, H. Hosono, *Iron-Based Layered Superconductor $La[O_{1-x}F_x]FeAs$ with Tc=26k*, Journal of the american chemical society, **130** (2008).

[14] V. Anisimov, J. Zaanen, O. Andersen, *Band theory and Mott insulators: Hubbard U instead of Stoner I*, Physical Review B, **44** (1991).

[15] M. Cococcioni S. Gironcoli, *Linear response approach to the calculation of the effective interaction parameters in the LDA+U method*, Physical Review B, **71** (2005).

[16] J. Hubbard, *Electron Correlation in Narrow Energy Bands*, Proceedings of the Royal Society A, **276** (1963).

[17] W. Metzner D. Vollhardt, *Correlated Lattice Fermions in d=inf Dimensions*, Physical Review Letters, **62** (1989).

[18] A. Georges, G. Kotliar, W. Krauth, M. Rozenberg, *Dynamical mean-field theory of strongly correlated fermion systems and the limit of infinite dimensions*, Reviews of modern physics, **68** (1996).

[19] M. Hettler, A. Tahvildar-Zadeh, M. Jarrell, T. Pruschke, H. Krishnamurthy, *Nonlocal dynamical correlations of strongly interacting electron systems*, Physical Review B, **58** (1998).

[20] A. Lichtenstein M. Katsnelson, *Antiferromagnetism and d-wave superconductivity in cuprates: A cluster dynamical mean-field theory*, Physical Review B, **62** (2000).

[21] G. Kotliar, S. Savrasov, G. Palsson, G. Biroli, *Cellular Dynamical Mean Field Approach to Strongly Correlated Systems*, Physical Review Letters, **87** (2001).

[22] T. Maier, M. Jarrell, T. Pruschke, M. Hettler, *Quantum cluster theories*, Reviews of modern physics, **77** (2005).

[23] A. N. Rubtsov, M. Katsnelson, A. Lichtenstein, *Dual fermion approach to nonlocal correlations in the Hubbard model*, Physical Review B, **77** (2008).

[24] S.-X. Yang, H. Terletska, Z. Meng, J. Moreno, M. Jarrell, *Mean-field embedding of the dual-fermion approach for correlated electron systems*, Physical Review B, **88** (2013).

[25] G. Rohringer, A. Toschi, H. Hafermann, K. Held, V. Anisimov, A. Katanin, *One-particle irreducible functional approach: A route to diagrammatic extensions of the dynamical mean-field theory*, Physical Review B, **88** (2013).

[26] C. Taranto, S. Andergassen, J. Bauer, K. Held, A. Katanin, W. Metzner, G. Rohringer, A. Toschi, *From infinite to two dimensions through the functional renormalization group*, arXiv (2013).

[27] A. Toschi, A. Katanin, K. Held, *Dynamical vertex approximation: A step beyond dynamical mean-field theory*, Physical Review B, **75** (2007).

[28] K. Held, A. Katanin, A. Toschi, *Dynamical Vertex Approximation: An Introduction*, Progress of Theoretical Physics Supplements, **176**, 117 (2008).

[29] E. Salpeter H. Bethe, *A Realtivistic Equation for Bound-State Problems*, Physical Review, **84** (1951).

[30] N. Lin, E. Gull, A. Millis, *Two-Particle Response in Cluster Dynamical Mean-Field Theory: Formalism and Application to the Raman Response of High-Temperature Superonductors*, Physical Review Letters, **109** (2012).

[31] H. Hafermann, *Self-energy and vertex functions from hybridization expansion continuous-time quantum Monte Carlo for impurity models with retarded interaction*, arXiv (2013).

[32] M. Kinza C. Honerkamp, *Two-particle correlations in a functional renormailzation group scheme using a dynamical mean-field theory approach*, Physical Review B, **88** (2013).

[33] J. Kuneš, *Efficient treatment of two-particle vertices in dynamical mean-field theory*, Physical Review B, **83** (2011).

[34] A. M. Zagoskin, *Quantum Theory of Many-Body Systems*, Springer (1998).

[35] A. L. Fetter J. Walecka, *Quantum Theory of Many-Particle Systems*, Dover (2003).

[36] A. Abrikosov, L. Gorkov, I. Dzyaloshinski, *Methods of quantum field theory in statistical physics*, Dover (1975).

[37] G. Kotliar, S. Savrasov, K. Haule, V. Oudovenko, O. Parcollet, C. Marianetti, *Electronic structure calculations with dynamical mean-field theory*, Reviews of modern physics, **78** (2006).

[38] J. Tomczak, A. Poteryaev, S. Biermann, *Momentum-resolved spectroscopcy of correlated metals: A view from dynamical mean field theory*, Comptes Rendus Physique, **10**, 537 (2009).

[39] J. Tomczak S. Biermann, *Optical properties of correlated materials - Or why intelligent windows may look dirty*, Physica Status Solidi B, **246**, 1996 (2009).

[40] G. Rohringer, A. Valli, A. Toschi, *Local Electronic Correlation at the two-particle level*, Physical Review B, **86** (2012).

[41] D. Senechal, *Theoretical Methods for Strongly Correlated Electrons*, Springer (2003).

[42] V. Janis, *Parquet approach to nonlocal vertex functions and electrical conductivity of disordered electrons*, Physical Review B, **64** (2001).

[43] K.-M. Tam, H. Fotso, S.-X. Yang, T.-W. Lee, J. Moreno, J. Ramanujam, M. Jarrell, *Solving the parquet equations for the Hubbard model beyond weak coupling*, Physical Review E, **87** (2013).

[44] G. Rohringer, *New routes towards a theoretical treatment of nonlocal electronic correlations*, , Vienna University of Technology (2014).

[45] H. Lehmann, *Ueber Eigenschaften von Ausbreitungsfunktionen und Renormierungskonstanten quantisierter Felder*, Nuovo Cimento, **11**, 342 (1954).

[46] N. Parragh, *A new scheme for LDA+DMFT calculations and algorithmic improvements for a multi-band DMFT-solver*, , Vienna University of Technology (2010).

[47] N. Ashcroft N. Mermin, *Solid State Physics*, Cengage Learning (1976).

[48] C. Goringe, D. Bowler, E. Hernandez, *Tight-binding modelling of materials*, Reports on Progress in Physics, **60** (1997).

[49] W. Harrison, *Electronic Structure and the Properteis of Solids: The Physics of the Chemical Bond*, Dover Publications (1989).

[50] J. de Boer E. Verwey, *Semi-conductors with partially and with completely filled 3d-lattice bands*, Proceedings of the Physical Society, **49** (1937).

[51] N. Mott, *Metal-Insulator Transition*, Reviews of modern physics, **40**, 677 (1968).

[52] A. Andreev I. Lifshitz, *Quantum Theory of Defects in Crystals*, Journal of Experimental and Theoretical Physics, **29** (1969).

[53] G.-S. Tian, *Particle-hole transformations and sum rules for the Hubbard model*, Physics Letters A, **228** (1997).

[54] R. Micnas, J. Ranninger, S. Robaszkiewicz, *Superconductivity in narrow-band systems with local nonretarded attractive interactions*, Reviews of modern physics, **62** (1990).

[55] T. Schaefer, G. Rohringer, O. Gunnarsson, S. Ciuchi, G. Sangiovanni, A. Toschi, *Divergent Precursors of the Mott-Hubbard Transition at the Two-Particle Level*, Physical Review Letters, **110** (2013).